Physica D 484 (2025) 134968

Contents lists available at ScienceDirect

Physica D

journal homepage: www.elsevier.com/locate/physd

Direct method phase-based model identification for coupled oscillators

Kaitlyn Toth [*], Dan Wilson

Department of Electrical Engineering and Computer Science, University of Tennessee, Knoxville, TN 37966, USA

ARTICLE INFO

Communicated by Victor M. Perez-Garcia

Keywords:
Phase reduction
Phase–amplitude reduction
Computational neuroscience
Data-driven techniques
Population-level analysis
Direct method

ABSTRACT

Phase-based reduction techniques are effective for the representation and analysis of limit cycle oscillators. In data-driven scenarios, the direct method is a well-established strategy that can be used to infer the phase dynamics of uncoupled oscillators. However, this strategy falls short when considering coupled oscillators. In this work, we investigate an extension of the direct method for inference of phase-based reduced order models that can explicitly accommodate coupling between limit cycle oscillators. Leveraging formal averaging theory, we determine approximate temporal dynamics for both phase and amplitude coordinates. We provide a step-by-step algorithm that details the derivation of terms for this reduced order model and demonstrate the utility of the proposed approach in a variety of examples that consider large populations of coupled neural oscillators.

1. Introduction

Phase-based reduction strategies are frequently used to model oscillatory dynamical systems of the general form

$$\dot{x} = F(x, u), \tag{1}$$

where $x \in \mathbb{R}^n$ defines the state and u is an applied input restricted to be $O(\epsilon)$ in magnitude, where $0 < \epsilon \ll 1$ [1–8]. Provided a T-periodic limit cycle x^γ exists, the n-dimensional system described in Eq. (1) can be represented in a reduced order framework using isochrons to define a reduced order coordinate system within the basin of attraction of the limit cycle [9–11]. For any two initial conditions, $a(0)$ and $b(0)$, in the basin of attraction, $\lim_{t\to\infty} \|a(t) - b(t)\| = 0$ if they are on the same isochron [2,11,12].

Simple phase reduction is often sufficient when the input $u(t)$ is small enough in magnitude that deviations from x^γ are small. Phase–amplitude reduction is an extension of phase reduction that utilizes Floquet theory to derive the dynamics of additional amplitude coordinates that account for perturbations transverse to the periodic orbit [12]. The resulting phase–amplitude reduced order model can be used to overcome some of the shortcomings of standard phase-based reduction strategies [13,14].

The necessary terms of the phase–amplitude reduction are computed straightforwardly when the underlying dynamical equations are known. When model equations are unavailable, they can be inferred from data using the direct method [11,15,16]. To implement the direct method, small pulse inputs are applied to estimate the phase sensitivity. It is essential that other unmodeled inputs such as coupling and noise do not significantly alter the phase. When considering a coupled system of oscillators, it is not possible to apply the direct method to infer the phase–amplitude reduced equation for the individual oscillators.

Previous research on data-driven model identification strategies for nonlinear dynamical systems utilize a variety of other techniques. For instance, dynamic mode decomposition (DMD) yields linear modes that represent snapshots of time-series data that can be analyzed with respect to associated eigenvalues and eigenvectors [17–21]. Since DMD yields a linear operator, however, it is often difficult to apply to systems with stable oscillations. Common machine learning approaches include the sparse identification of nonlinear dynamics (SINDy) algorithm, which implements sparse regression to find candidate functions that best reflect a given system's temporal dynamics [22,23]. However since the SINDy algorithm considers best candidate functions, these functions may not always reflect the true dynamics or structure of a system and its coupling. Additionally, with machine learning, overfitting is a concern. Deep learning and neural networks can be applied to infer the dynamics of nonlinear dynamical systems from data [24–27]. However, similar to traditional machine learning, overfitting can again be an issue, and the black box nature of deep learning models implies that any derived coupling structure within the system may not be accurate or fully understood. Data-driven approaches to phase-based model reduction have also been considered in previous works. In [28], proper orthogonal decomposition was applied to observable data to infer the parameters for a phase–amplitude reduced order model. In [29], the authors derive a phase–amplitude model using the aforementioned direct method by strategically applying external inputs to a system and measuring the system's sensitivity to perturbations at different

---

[*] Corresponding author.
E-mail address: ktoth3@utk.edu (K. Toth).

https://doi.org/10.1016/j.physd.2025.134968
Received 29 April 2025; Received in revised form 15 August 2025; Accepted 29 September 2025

states along its limit cycle. In [30], the authors implement deep learning and artificial neural networks to determine relevant terms for a phase–amplitude reduced order model.

In this work, we extend the direct method to explicitly consider a population of coupled limit cycle oscillators. Using observables from these systems, we propose a strategy to infer relevant parameters for their corresponding phase-based reduced order models. While the approach presented here can be practically applied to a variety of coupled oscillator systems, we are motivated by its possible use as an aid in the understanding of coupled neural rhythms. Functional connections of the brain have been studied for decades [31,32]. Many of these studies are motivated by the potential to understand the efficacy of treatments for certain neurological or psychiatric conditions where the only true observables are the manifestation or disappearance of related symptoms [33]. Findings indicate that brain rhythms play an important role in cognitive function, and abnormal brain rhythms are related to the onset of certain neurological disorders [34]. Excessive synchronization of neurons, for instance, is observed in patients with Parkinson's disease and the disruption of this synchronization through deep brain stimulation (DBS) alleviates the associated tremors [34–38]. Motivated by the potential applications of data-driven reduced order modeling in coupled oscillator networks such as those often studied in computational neuroscience, we present here a data-driven method that extends the direct method to produce a phase-based reduced order model that accounts for complex coupling structures between oscillators.

The remainder of this paper is organized as follows. In Section 2, we describe the phase–amplitude reduced order model, its limitations, and its underlying assumptions and derive an analytical model that will form the basis of the data-driven algorithm. In Section 3, we provide a detailed algorithm for inferring the necessary terms of the reduced order model from data. Section 4 provides results for a simple coupled two oscillator system. Section 5 gives an overview of the study of population-level oscillations for neural models. Sections 6 and 7 give results for the proposed model identification strategy applied to population-level oscillations of a two subnetwork (Section 6) and four subnetwork (Section 7) system of neural oscillators. Section 8 explores limitations of this model identification strategy that arise due to coupling structure and oscillator observability. Concluding remarks are provided in Section 9.

2. The phase-amplitude reduced order model

2.1. Background

Consider a general nonlinear dynamical system of the form (1), where x is the state as determined by the system's internal dynamics and u is an external input. Provided a T-periodic limit cycle x^γ exists, the timing of the oscillations in (1) can be considered using phase reduction. Transforming to phase coordinates, the dynamics are:

$$\begin{aligned}\dot{\theta} &= \frac{\partial \theta}{\partial x} \cdot \dot{x}, \\ &= \frac{\partial \theta}{\partial x} \cdot F(x,u), \\ &= \frac{\partial \theta}{\partial x} \cdot \left(F(x,0) + \frac{\partial F}{\partial u} u + O(|u|^2)\right), .\end{aligned} \tag{2}$$

Simplifying Eq. (2) further and dropping higher order terms yields a standard phase reduced model:

$$\dot{\theta} = \omega + \epsilon Z(\theta) u(t), \tag{3}$$

where $\omega = 2\pi/T$ is the natural frequency of the limit cycle oscillator and $Z(\theta) = \frac{\partial \theta}{\partial x}^T \frac{\partial F}{\partial u}$ is the infinitesimal phase response curve evaluated along the limit cycle at phase θ.

The addition of amplitude coordinates in a reduced order model can account for perturbations from the limit cycle which decay slowly back towards the periodic orbit [12]. Amplitude coordinates can be included by considering level sets of the slowest decaying eigenmodes of the Koopman operator [39,40]. One such approach uses the isostable coordinate system, leveraging Floquet theory to capture transient dynamics in directions transverse to the limit cycle. We define $\lambda = \exp(\kappa T)$ to be the smallest nonunity eigenvalue of the fundamental matrix, Φ, associated with the dynamical system in Eq. (1), where $x(T) = \Phi x(0)$ for an initial solution x(0) [13]. The slowest decaying isostable coordinate is defined within the basin of attraction of a limit cycle according to

$$\psi(x) = \lim_{k\to\infty} \left(w^T \left(\nu(t_\Gamma^k, x) - x_0 \right) \exp(-\kappa t_\Gamma^k) \right), \tag{4}$$

where w^T is the left eigenvector of the fundamental matrix Φ associated with the slowest decaying Floquet exponent κ, t_Γ^k indicates the time of the kth crossing of the $\theta = 0$ isochron Γ_0, $\nu(t_\Gamma^k, x)$ is the flow of the dynamical system defined in Eq. (1), and x_0 denotes the location where Γ_0 intersects the periodic orbit. As k approaches infinity, Eq. (4) converges to the isostable coordinate. The dynamics of the isostable coordinate for a single oscillator are:

$$\begin{aligned}\dot{\psi} &= \frac{\partial \psi}{\partial x} \cdot \dot{x}, \\ &= \frac{\partial \psi}{\partial x} \cdot F(x,u), \\ &= \frac{\partial \psi}{\partial x} \cdot \left(F(x,0) + \frac{\partial F}{\partial u} u + O(|u|^2)\right).\end{aligned} \tag{5}$$

Simplifying Eq. (5) and dropping the higher order terms yields

$$\dot{\psi} = \kappa \psi + \epsilon I(\theta) u(t), \tag{6}$$

where κ is the slowest decaying Floquet exponent and $I(\theta) = \frac{\partial \psi}{\partial x}^T \frac{\partial F}{\partial u}$ is the isostable response curve evaluated along the limit cycle at each phase θ. For additional information on isostable reduction, and a complete derivation and explanation of terms, please refer to [12,13]. To linear orders of accuracy, isostable coordinates are the same as Floquet coordinates. In a close neighborhood of the limit cycle, i.e., when ψ is small, the state of (1) can be represented using phase–amplitude reduction and can be written as a function of θ and ψ:

$$x(t) = x\big(\theta(t), \psi(t)\big) = x^\gamma\big(\theta(t)\big) + \psi(t) g\big(\theta(t)\big), \tag{7}$$

where $x^\gamma\big(\theta(t)\big)$ is the stable limit cycle of (1) and $g\big(\theta\big)$ is 2π-periodic [13].

Fig. 1 considers an illustration of (7) with a toy example. Here, let x_1 be the first component of x and $x_1^\gamma\big(\theta\big) = \sin\big(\theta\big)$ and $g_1\big(\theta\big) = \cos\big(\theta\big)$ be the first components of x^γ and g, respectively. In the absence of input, $\psi(t) = \psi_0 \exp(\kappa t)$ and $\theta(t) = \omega t + \theta_0$ where θ_0 and ψ_0 are initial conditions. Here, we take $\kappa = -0.2$ and $\omega = 1$. First consider two different trajectories starting at identical phases but with different ψ_0 values in Panel A of Fig. 1. These trajectories converge to each other, with the distance to the periodic orbit depending on ψ. Notably, these trajectories converge to the same phase along the limit cycle but at different rates. Next consider two different trajectories starting at different initial phases but with identical ψ_0 values (Panel B). The distance from the periodic orbit is roughly the same as a function of time, but the oscillation timing is different between oscillators. Therefore, these trajectories converge to the limit cycle at the same rate but approach different phases. In this plot, two variations of x^γ are shown corresponding to the two initial phases of the red and blue trajectories. Panel C shows trajectories starting at different initial phases with different ψ_0. These trajectories approach the limit cycle at different rates and converge to different phases. Again, two variations of x^γ are shown with different initial phases.

2.2. Phase and amplitude dynamics for a coupled population of oscillators

Consider a population of N coupled limit cycle oscillators with dynamics that can be written in the form

$$\dot{\theta}_i = \omega_i + \epsilon \sum_{k\neq i} Z_i(\theta_i) g_{k\to i}(\theta_i, \theta_k), \tag{8}$$

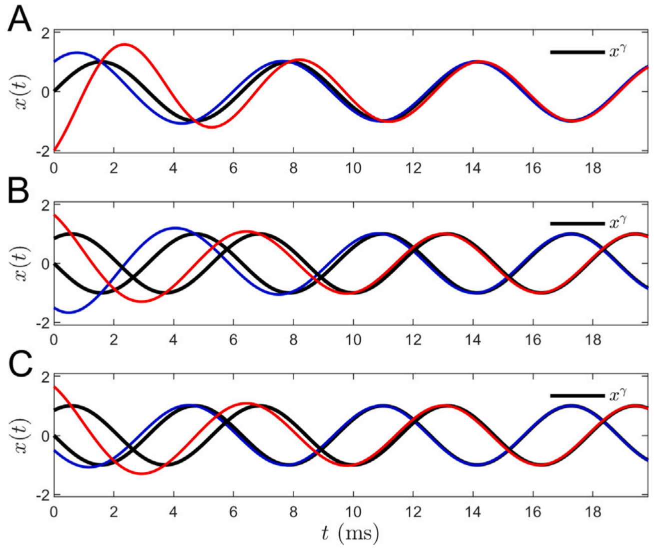

Fig. 1. An illustration of (7) for a toy system. Panel A: initial conditions with different isostable coordinates but the same phase. Panel B: same isostable coordinate, different phase. Panel C: different initial phase and isostable coordinates.

$$\dot{\psi}_i = \kappa_i \psi_i + \epsilon \sum_{k \neq i} I_i(\theta_i) g_{k\to i}(\theta_i, \theta_k),$$

for $i = 1, \dots, N$ where g sets the coupling. Here, $0 < \epsilon \ll 1$ so that the influence of coupling is small relative to the natural frequency of the oscillators. The oscillators are coupled in an all-to-all fashion with no self coupling. It is assumed that each κ_i is an order ϵ term, i.e., so that the amplitude coordinates decay slowly. Defining $\phi_{i,j} = \theta_i - \theta_j$, Eq. (8) can be rewritten as

$$\begin{aligned} \dot{\theta}_i &= \omega_i + \epsilon \sum_{k \neq i} Z_i(\theta_i) g_{k\to i}(\theta_i, \theta_i - \phi_{i,k}), \\ \dot{\psi}_i &= \kappa_i \psi_i + \epsilon \sum_{k \neq i} I_i(\theta_i) g_{k\to i}(\theta_i, \theta_i - \phi_{i,k}), \\ & i = 1, \dots, N. \end{aligned} \tag{9}$$

We seek to transform (9) to a function of the form $\dot{x} = \epsilon f(x,t)$ in order to employ dynamical averaging [41,42], but since ω_i in (9) is not an order ϵ term, we cannot perform dynamical averaging without an intermediate step. We define the phase difference between any two oscillators, i and j, to have associated dynamics defined to be $\dot{\phi}_{i,j} = \dot{\theta}_i - \dot{\theta}_j$ so that

$$\dot{\phi}_{i,j} = \omega_i - \omega_j + \epsilon \sum_{k \neq i} Z_i(\theta_i) g_{k\to i}(\theta_i, \theta_i - \phi_{i,k}) - \epsilon \sum_{k \neq j} Z_j(\theta_j) g_{k\to j}(\theta_j, \theta_j - \phi_{j,k}). \tag{10}$$

Provided $\omega_i - \omega_j = O(\epsilon)$, the right hand side of (10) is an order ϵ term and we can apply formal dynamical averaging techniques [41,42]. We will work in a rotating reference frame by defining a new phase variable,

$$\zeta_i = \theta_i - \omega_0 t, \tag{11}$$

where $\omega_0 = \frac{1}{N} \sum_{i=1}^{N} \omega_i$ is the average natural frequency of the population of N oscillators. Note that $\phi_{i,j} = \theta_i - \theta_j = \zeta_i - \zeta_j$. Rewriting Eq. (9) in this rotating reference frame yields

$$\begin{aligned} \dot{\zeta}_i &= \omega_i - \omega_0 + \epsilon \sum_{k \neq i} Z_i(\zeta_i + \omega_0 t) g_{k\to i}(\zeta_i + \omega_0 t, \zeta_k + \omega_0 t), \\ \dot{\psi}_i &= \kappa_i \psi_i + \epsilon \sum_{k \neq i} I_i(\zeta_i + \omega_0 t) g_{k\to i}(\zeta_i + \omega_0 t, \zeta_k + \omega_0 t), \\ & i = 1, \dots, N. \end{aligned} \tag{12}$$

Averaging the dynamics defined in Eq. (12) over the period $T_0 = 2\pi/\omega_0$ and defining $\Delta\omega_i = \omega_i - \omega_0$ yields

$$\begin{aligned} \dot{\zeta}_i^* &= \frac{1}{T_0} \int_0^{T_0} \left[\Delta\omega_i + \epsilon \sum_{k \neq i} Z_i(\zeta_i^* + \omega_0 t) g_{k\to i}(\zeta_i^* + \omega_0 t, \zeta_k^* + \omega_0 t) \right] dt, \\ \dot{\psi}_i^* &= \frac{1}{T_0} \int_0^{T_0} \left[\kappa_i \psi_i^* + \epsilon \sum_{k \neq i} I_i(\zeta_i^* + \omega_0 t) g_{k\to i}(\zeta_i^* + \omega_0 t, \zeta_k^* + \omega_0 t) \right] dt, \\ & i = 1, \dots, N, \end{aligned} \tag{13}$$

where $\zeta_i^* \approx \zeta_i$ since solutions of (12) are well approximated by solutions of the averaged Eq. (13). Factoring out the constant terms from the integrands in Eq. (13) and exchanging the summation and integration order yields

$$\begin{aligned} \dot{\zeta}_i^* &= \Delta\omega_i + \epsilon \sum_{k \neq i} \frac{1}{T_0} \int_0^{T_0} \left[Z_i(\zeta_i^* + \omega_0 t) g_{k\to i}(\zeta_i^* + \omega_0 t, \zeta_k^* + \omega_0 t) \right] dt, \\ \dot{\psi}_i^* &= \kappa_i \psi_i^* + \epsilon \sum_{k \neq i} \frac{1}{T_0} \int_0^{T_0} \left[I_i(\zeta_i^* + \omega_0 t) g_{k\to i}(\zeta_i^* + \omega_0 t, \zeta_k^* + \omega_0 t) \right] dt, \\ & i = 1, \dots, N. \end{aligned} \tag{14}$$

Considering Eq. (14), we define coupling functions between any two oscillators, i and k:

$$\begin{aligned} \Gamma_{\zeta,k\to i}(\phi_{i,k}) &= \frac{\epsilon}{T_0} \int_0^{T_0} \left[Z_i(\zeta_i + \omega_0 t) g_{k\to i}(\zeta_i + \omega_0 t, \zeta_k + \omega_0 t) \right] dt, \\ \Gamma_{\psi,k\to i}(\phi_{i,k}) &= \frac{\epsilon}{T_0} \int_0^{T_0} \left[I_i(\zeta_i + \omega_0 t) g_{k\to i}(\zeta_i + \omega_0 t, \zeta_k + \omega_0 t) \right] dt. \end{aligned} \tag{15}$$

Note that because of the integration over an entire period, $\Gamma_{\zeta,k\to i}$ and $\Gamma_{\psi,k\to i}$ are functions of only $\phi_{i,k}$. Substituting (15) into (14), and considering that $\zeta_i \approx \zeta_i^*$ and $\psi_i \approx \psi_i^*$, one finds

$$\begin{aligned} \dot{\zeta}_i &= \Delta\omega_i + \sum_{k \neq i} \Gamma_{\zeta,k\to i}(\phi_{i,k}), \\ \dot{\psi}_i &= \kappa_i \psi_i + \sum_{k \neq i} \Gamma_{\psi,k\to i}(\phi_{i,k}), \end{aligned} \tag{16}$$

for $i = 1, \dots, N$ oscillators.

3. Data-driven model identification for the phase dynamics of the coupled oscillator model

3.1. Defining the data-driven basis function

The coupling functions, $\Gamma_{\zeta,k\to i}(\phi_{i,k})$ and $\Gamma_{\psi,k\to i}(\phi_{i,k})$, are periodic over the range $\phi = [0, 2\pi)$ and can therefore be approximated using the M^{th} order Fourier series expansion

$$\begin{aligned} \Gamma_{\zeta,k\to i}(\phi_{i,k}) &\approx \frac{a_{0,k\to i}}{2} + \sum_{n=1}^{M} a_{n,k\to i} \sin(n\phi_{i,k}) + b_{n,k\to i} \cos(n\phi_{i,k}), \\ \Gamma_{\psi,k\to i}(\phi_{i,k}) &\approx \frac{c_{0,k\to i}}{2} + \sum_{n=1}^{M} c_{n,k\to i} \sin(n\phi_{i,k}) + d_{n,k\to i} \cos(n\phi_{i,k}). \end{aligned} \tag{17}$$

If the $\phi_{i,k}$ values that are obtained from data are not measured over the entire range of possible phase differences $\big(\phi \in [0, 2\pi)\big)$, Eq. (17) cannot yield an accurate approximation of the coupling dynamics. In these cases, it is likely that the oscillators themselves possess either a strong antiphase tendency (measurements of $\phi_{i,k}$ are clustered around π) or a strong synchronizing tendency (measurements of $\phi_{i,k}$ are clustered around 0 and 2π). In the case of population-level dynamics (which will be discussed later), it is also possible that these population-level dynamics are close to the threshold of complete desynchronization. In these situations, the actual coupling functions are still periodic over the range $\phi \in [0, 2\pi)$, but the observables would not provide a complete picture of the true coupling functions.

We write the dynamics in Eq. (16) using a Fourier series expansion by including two additional terms, $\Delta\omega_i$ and $\kappa_i\psi_i$. Substituting the Fourier series representation in (17) into (16) yields

$$\dot{\zeta}_i \approx \Delta\omega_i + \hat{a}_{0,i} + \sum_{k\neq i}\sum_{n=1}^{M} a_{n,k\to i}\sin(n\phi_{i,k}) + b_{n,k\to i}\cos(n\phi_{i,k}), \tag{18}$$

$$\dot{\psi}_i \approx \kappa_i\psi_i + \hat{c}_{0,i} + \sum_{k\neq i}\sum_{n=1}^{M} c_{n,k\to i}\sin(n\phi_{i,k}) + d_{n,k\to i}\cos(n\phi_{i,k}),$$

$$i = 1,\dots,N,$$

where $\hat{a}_{0,i} = \frac{1}{2}\sum_{k\neq i} a_{0,k\to i}$ and $\hat{c}_{0,i} = \frac{1}{2}\sum_{k\neq i} c_{0,k\to i}$. Recall again that using the weak coupling assumption, $\dot{\phi}_{i,k} = O(\epsilon)$ while $\dot{\theta}_i = O(1)$ so that each $\phi_{i,k}$ changes slowly on the timescale of a single oscillator's period and can be approximated by a constant. The averaged values can therefore be used to approximate the unaveraged values of $\dot{\zeta}_i$ and $\dot{\psi}_i$ [41,42]. Finally, we convert back to θ_i by substituting $\theta_i = \zeta_i + \omega_0 t$. We also determine some measurable value ν that varies each cycle between $\theta = 0$ isochron crossings to model the dynamics of each oscillator's isostable coordinate. This amplitude coordinate and the actual isostable coordinate have a linear relationship so that $\nu_i = p_i\psi_i$, where p_i is a constant. This value can, for instance, be the difference between the local maximum and the local minimum over a given cycle, as is represented in Fig. 2 for a two oscillator model. The linear relationship $\nu_i = p_i\psi_i$ is valid provided perturbations to the system are small in magnitude. We assume that the decay rate is small enough so that the isostable coordinate can be well approximated by a constant over a single cycle. With these assumptions, it follows that ν is dependent only on time and not on phase. Using the coordinate change $\nu_i = p_i\psi_i$, these substitutions yield a phase-based model that we will obtain using a data-driven approach:

$$\dot{\theta}_i = \omega_i + \hat{a}_{0,i} + \sum_{k\neq i}\sum_{n=1}^{M} a_{n,k\to i}\sin(n\phi_{i,k}) + b_{n,k\to i}\cos(n\phi_{i,k}), \tag{19}$$

$$\dot{\nu}_i = \kappa_i\nu_i + \frac{\hat{c}_{0,i}}{p_i} + \sum_{k\neq i}\sum_{n=1}^{M} \frac{c_{n,k\to i}}{p_i}\sin(n\phi_{i,k}) + \frac{d_{n,k\to i}}{p_i}\cos(n\phi_{i,k}),$$

$$i = 1,\dots,N.$$

The original state in the full order model can be inferred from the reduced order dynamics since $x = f(\theta,\nu)$ where $f(\theta,\nu)$ can be inferred using (7). Note that while p_i is usually unknown, it is only necessary to determine the ratios $\frac{\hat{c}_{0,i}}{p_i}$, $\frac{c_{n,k\to i}}{p_i}$, $\frac{d_{n,k\to i}}{p_i}$ in the inference of (19).

3.2. The data driven model: An algorithm

The unknown coefficients from (19) can be approximated with the linear matrix equations

$$B_1 = A_1 F_1, \tag{20}$$

$$B_2 = A_2 F_2.$$

Using a first order Fourier series approximation, for m discrete time steps and i coupled to $k = 1,\dots,q$ oscillators, $B_1 \in R^{m\times 1}$, $A_1 \in R^{m\times(2q+1)}$, and $F_1 \in R^{(2q+1)\times 1}$ are defined below

$$B_1 = \begin{bmatrix}\dot{\theta}_i(t_1) & \cdots & \dot{\theta}_i(t_m)\end{bmatrix}^T, \tag{21}$$

$$A_1 = \begin{bmatrix} 1 & \sin(\phi_{i,1}(t_1)) & \cos(\phi_{i,1}(t_1)) & \cdots & \sin(\phi_{i,q}(t_1)) & \cos(\phi_{i,q}(t_1)) \\ \vdots & \vdots & \vdots & \vdots & \vdots & \vdots \\ 1 & \sin(\phi_{i,1}(t_m)) & \cos(\phi_{i,1}(t_m)) & \cdots & \sin(\phi_{i,q}(t_m)) & \cos(\phi_{i,q}(t_m)) \end{bmatrix},$$

$$F_1 = \begin{bmatrix}(\omega_i + \hat{a}_{0,i}) & a_{1,1\to i} & b_{1,1\to i} & \cdots & a_{1,q\to i} & b_{1,q\to i}\end{bmatrix}^T,$$

and $B_2 \in R^{m\times 1}$, $A_2 \in R^{m\times(2q+2)}$, and $F_2 \in R^{(2q+2)\times 1}$ are defined as

$$B_2 = \begin{bmatrix}\dot{\nu}_i(t_1) & \cdots & \dot{\nu}_i(t_m)\end{bmatrix}^T, \tag{22}$$

$$A_2 = \begin{bmatrix} \nu_i(t_1) & 1 & \sin(\phi_{i,1}(t_1)) & \cos(\phi_{i,1}(t_1)) & \cdots & \sin(\phi_{i,q}(t_1)) & \cos(\phi_{i,q}(t_1)) \\ \vdots & \vdots & \vdots & \vdots & \vdots & \vdots & \vdots \\ \nu_i(t_m) & 1 & \sin(\phi_{i,1}(t_m)) & \cos(\phi_{i,1}(t_m)) & \cdots & \sin(\phi_{i,q}(t_m)) & \cos(\phi_{i,q}(t_m)) \end{bmatrix},$$

$$F_2 = \begin{bmatrix}\kappa_i & \frac{\hat{c}_{0,i}}{p_i} & \frac{c_{1,1\to i}}{p_i} & \frac{d_{1,1\to i}}{p_i} & \cdots & \frac{c_{1,q\to i}}{p_i} & \frac{d_{1,q\to i}}{p_i}\end{bmatrix}^T.$$

In B_1 and B_2, the discrete approximations of $\dot{\theta}(t)$ and $\dot{\nu}(t)$ are determined by fluctuations in the time and state between crossings of some reference isochron. The discrete approximations of ν_i and $\phi_{i,k}$ can also be made by analyzing the time and state between crossings of some reference isochron. Therefore in a data-driven setting, F_1 and F_2 are the only unknowns while the elements of B_1, B_2, A_1, and A_2 can be determined from data. In (21) and (22), only the first modes of the Fourier series expansions are computed for each coupling function. Additional modes can be obtained with appropriate modifications to A_1, A_2, F_1, and F_2.

A step-by-step explanation of how to estimate the elements of A_1, A_2, B_1, and B_2 and develop a phase–amplitude model in the form of Eq. (19) using a least-squares approximation of the Fourier series coefficients is provided in the algorithm below.

1. Simulate the full order model (Eq. (1)) for an extended period of time (approximately 50–100 oscillations). Determine a set of observables from which to obtain measurement data. Each oscillator must have a stable limit cycle.
2. Define some value of each observable to represent the $\theta = 0$ isochron in the phase space for each oscillator. The $\theta = 0$ isochron can correspond, for instance, to the occurrence of a local minimum or maximum or to the crossing of a Poincaré section as in Figs. 2 and 3.
3. Extract each cycle of the chosen observables between crossings of the $\theta = 0$ isochron. These cycles are stored as vectors that contain the states of the system from one crossing of the $\theta = 0$ isochron to the next subsequent crossing of the $\theta = 0$ isochron. In a stable, unperturbed, periodic system, each cycle would simply be the periodic orbit.
4. For each limit cycle oscillator, define the time of crossings of the $\theta = 0$ isochron by the chosen observable to be $t_1, t_2, \dots, t_{N_{cross}}$ and the time between crossings to be $T_1 = (t_2 - t_1), T_2 = (t_3 - t_2), \dots, T_{N_{cross}-1} = (t_{N_{cross}} - t_{N_{cross-1}})$ where N_{cross} is the total number of isochron crossings. Fig. 3 illustrates these terms for a single example cycle.
5. For each limit cycle oscillator, define a chosen amplitude coordinate and calculate the amplitude for each cycle between

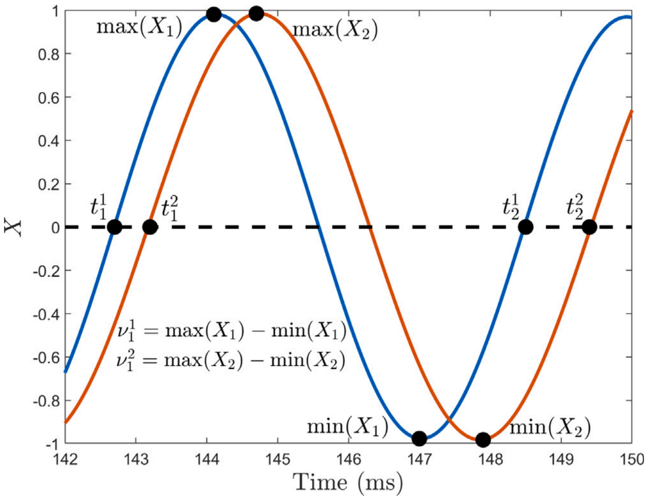

Fig. 2. This figure demonstrates the calculation of $\nu_k = \max(X) - \min(X)$ over a single cycle for example data. Here, ν_k is an amplitude coordinate that is proportional to the system's slowest decaying isostable coordinate. In this figure, we only plot two crossings of the $\theta = 0$ isochron for each oscillator (t_k^1 and t_k^2) and obtain an amplitude coordinate for the corresponding cycle between those crossings.

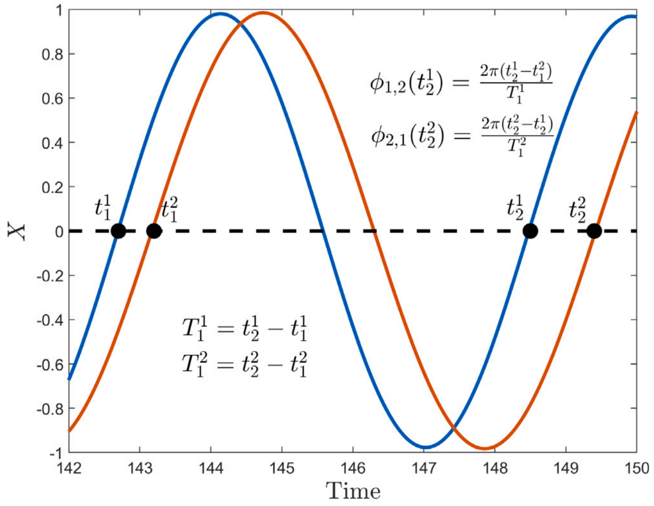

Fig. 3. This figure demonstrates the determination of t_k, T_k, and $\phi_{i,j}(t_k)$ for example data. In this figure, we only plot two crossings of the $\theta = 0$ isochron for each oscillator (t_k^1 and t_k^2).

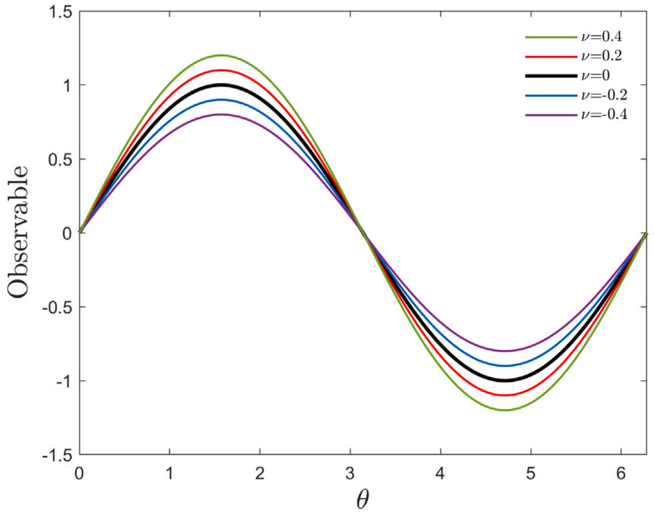

Fig. 4. This figure demonstrates the relationship between the observable of the full order model, θ, and ν. The observable is a sinusoidal wave with an associated amplitude shown over the range $\theta \in [0, 2\pi)$. To infer the observable from the reduced order model, one would interpolate using the available cycles with the closest ν values and the phase.

crossings of the $\theta = 0$ isochron. Define the amplitudes to be $\nu_1, \dots, \nu_{N_{cross}-1}$. Fig. 2 illustrates this calculation for a single example cycle.

6. Use the time between crossings from Step 4 to approximate instantaneous measurements of $\dot{\theta}_i$ for each oscillator i. Store these measurements in the vector B_1,

$$B_1 = \left[\frac{2\pi}{T_1}, \frac{2\pi}{T_2}, \dots, \frac{2\pi}{T_{N_{cross}-1}} \right]^T. \tag{23}$$

7. Use the time between crossings from Step 4 and the amplitudes from Step 5 to define discrete measurements of $\dot{\nu}_i$ for each oscillator i. Store these measurements in the vector B_2,

$$B_2 = \left[\frac{\nu_2 - \nu_1}{T_1}, \frac{\nu_3 - \nu_2}{T_2}, \dots, \frac{\nu_{N_{cross}-1} - \nu_{N_{cross}-2}}{T_{N_{cross}-1}} \right]^T. \tag{24}$$

8. Define the phase difference between any two oscillators, i and j, at each isochron crossing k to be $\phi_{i,j}(t_k) = [2\pi \min(t_k^i - t^j)]/T_k^i$, where t_k^i is the kth crossing by oscillator i of the $\theta = 0$ isochron, t^j are all crossings of the $\theta = 0$ isochron by oscillator j that occur before t_k^i, and $T_k^i = t_k^i - t_{k-1}^i$. Thus, we are solving for the closest crossing of the $\theta = 0$ isochron to t_k^i by oscillator j that occurs up to the time t_k^i. An example of this calculation for a single cycle of the $\theta = 0$ isochron can be found in Fig. 3. It is necessary to have measurements of $\phi_{i,j}$ over the entire range of possible phase differences $[0, 2\pi)$.
9. For each oscillator i: using the phase differences found in Step 8, set up matrix A_1 from Eq. (21) using $m = N_{cross} - 1$ rows of Fourier series terms up to the desired order.
10. For each oscillator i: using the phase differences found in Step 8 and the amplitude values found in Step 5, set up matrix A_2 from Eq. (22) using $m = N_{cross} - 1$ rows of Fourier series terms up to the desired order.
11. To determine the Fourier series coefficients for the phase dynamics, use Eq. (20) with the B_1 vector from Step 6 and the A_1 matrix from Step 9 to solve for F_1:

$$F_1 = A_1^{\dagger} B_1. \tag{25}$$

Here † indicates a pseudoinverse.

12. To determine the Fourier series coefficients for the amplitude dynamics, use Eq. (20) with the B_2 vector from Step 7 and the A_2 matrix from Step 10 to solve for F_2:

$$F_2 = A_2^{\dagger} B_2. \tag{26}$$

Here † again indicates a pseudoinverse.

13. Run the phase–amplitude reduced order model defined in Eq. (19) using the Fourier series coefficients stored in F_1 and F_2. Within the reduced order model, calculate the phase difference instantaneously.
14. To verify the efficacy of the reduced order model, map back to equivalent states in the full order model using the amplitude and phase coordinates to infer corresponding states in the full order model. This is possible analytically since the state can be inferred from the phase and isostable coordinate, as is represented in (7). For a practical representation of how to infer the state from the reduced order model numerically, refer to Fig. 4. The combination of the amplitude coordinate and the phase can be used to infer the state of the observable in the full order model.

4. Example with a simple model: the nonradial isochron clock

To illustrate the efficacy of our technique, we consider a simple model of two coupled oscillators of the form:

$$\begin{aligned} \dot{X}_i &= C_i \sigma X_i \left(\mu - (X_i^2 + Y_i^2) \right) - Y_i \Big(C_i \big(1 + \rho (X_i^2 + Y_i^2 - \mu) \big) \Big) \\ &\quad - \frac{\beta}{N-1} \sum_{j \neq i}^{N} (X_i - X_j), \\ \dot{Y}_i &= C_i \sigma Y_i \left(\mu - (X_i^2 + Y_i^2) \right) + X_i \Big(C_i \big(1 + \rho (X_i^2 + Y_i^2 - \mu) \big) \Big), \\ i &= 1, 2. \end{aligned} \tag{27}$$

This equation is a modified version of Winfree's radial isochron clock [11] with added diffusive coupling. Here, $C_1 = 1.1$ and $C_2 = 1.0$ are constants that explicitly define the stable natural frequencies of the uncoupled oscillators: $\omega_1 = C_1 = 2\pi/T_1$ and $\omega_2 = C_2 = 2\pi/T_2$ where T_1 and T_2 are the associated stable periods of the uncoupled system. The parameters of the system are defined to be $\sigma = 0.08$, $\rho = 0.12$,

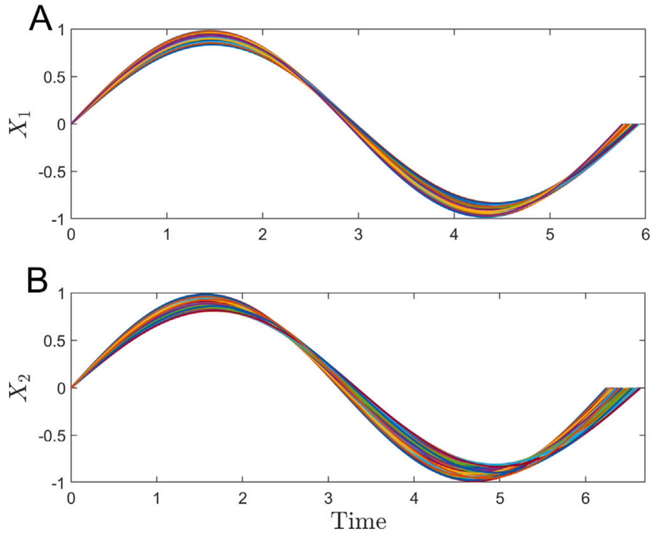

Fig. 5. Cycles of the observables for the coupled two oscillator dynamics of the nonradial isochron clock. Panel A plots these cycles for the first oscillator and panel B plots these cycles for the second oscillator.

and $\mu = 1$. The coupling strength between the oscillators is $\beta = 0.03$. Following the steps listed in Section 3.2, we will infer a data-driven phase–amplitude model that accurately captures the dynamics of (27).

4.1. Fitting the model to data

To begin, we simulate (27) for 600 time units. Defining the $\theta = 0$ isochron to be when both $X = 0$ and $\dot{X} > 0$ for a given oscillator, we extracted the individual cycles between isochron crossings. These cycles are plotted in Fig. 5 for oscillator 1 in panel A and oscillator 2 in panel B.

Using this data, we found discrete approximations of $\dot{\theta}_i$, $\dot{v}_i$, v_i and $\phi_{i,j}$ and defined A_1, B_1, A_2, and B_2 for each oscillator i following Steps 4–10 of Section 3.2. In this application, we defined the amplitude coordinate of the ith oscillator to be $v_k^i = \max(X_k^i) - \min(X_k^i) - v_{0,i}$ for each kth cycle between crossings of the $\theta = 0$ isochron. In this equation, $v_{0,i} = \frac{1}{N_{cross}-1}\sum_{k=1}^{N_{cross}-1}\left(\max(X_k^i) - \min(X_k^i)\right)$. With the B_1 vector and A_1 matrix, we evaluated Eq. (25) and determined the Fourier series coefficients that govern the phase dynamics. With the B_2 vector and A_2 matrix, we then evaluated Eq. (26) and determined the Fourier series coefficients that govern the amplitude dynamics. The F_1 and F_2 vectors contain the Fourier series coefficients that are used in the phase–amplitude model defined in Eq. (19). In this example, we used a first-order Fourier series approximation.

Fig. 6 presents a direct comparison between the measured observables $B_1 \approx \dot{\theta}_i(t_k)$ as defined in Eq. (23) and the evaluation of A_1F_1 from Eq. (25). Similarly, Fig. 7 presents a comparison between the measured observables $B_2 \approx \dot{v}_i(t_k)$ from Eq. (24) and the evaluation of A_2F_2 from Eq. (26). These are plotted over the range of phase differences used in the terms of the A_1 and A_2 matrices in Eqs. (21) and (22). In both figures, the observable data $\dot{\theta}_i$ and $\dot{v}_i$ is shown in blue and the approximations using A_1F_1 and A_2F_2 are in black. In both figures, panel A presents the information for the first oscillator and panel B presents it for the second oscillator.

4.2. Comparisons between ground truth and inferred model simulations

To test the model, we simulated Eq. (19) using the derived Fourier series coefficients found using Eqs. (25) and (26). The phase and amplitude coordinates for this simulation are shown in Fig. 8 for a snapshot of 200 time units.

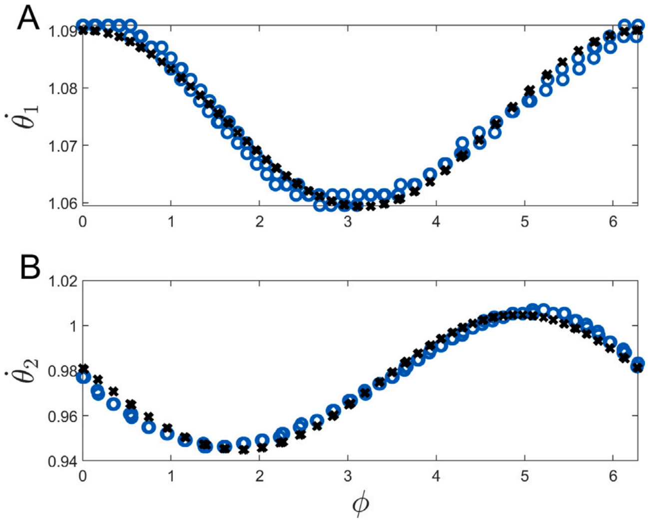

Fig. 6. This figure validates the least-squares approximation of the Fourier series coefficients for the phase dynamics derived in Section 3.2. It directly compares the measured data defined in Eq. (23) with the evaluation of A_1F_1, where A_1 and F_1 are calculated using the steps in Section 3.2. These are plotted as a function of the phase difference $\phi_{i,k}$ calculated in Step 8 of Section 3.2 and found in the terms of the A_1 matrix. The measured data from Eq. (23) is shown in blue and the data obtained from the evaluation of A_1F_1 is shown in black. Panel A presents these results for the first oscillator and panel B presents these results for the second oscillator.

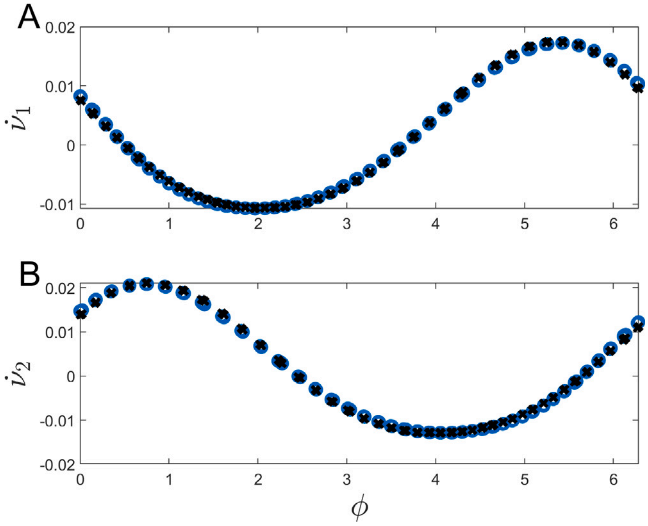

Fig. 7. This figure validates the least-squares approximation of the Fourier series coefficients for the amplitude dynamics derived in Section 3.2. It directly compares the measured data defined in Eq. (24) with the evaluation of A_2F_2, where A_2 and F_2 are calculated using the steps in Section 3.2. These are plotted as a function of the phase difference $\phi_{i,k}$ calculated in Step 8 of Section 3.2 and found in the terms of the A_2 matrix. The measured data from Eq. (24) is shown in blue and the data obtained from the evaluation of A_2F_2 is shown in black. Panel A presents these results for the first oscillator and panel B presents these results for the second oscillator.

We compare the ground truth model with the phase-based model by approximating identical initial conditions of the full order model in the phase space and evolving the phase-based model defined in Eq. (19) forward in time. We present a comparison of the two simulations in Fig.

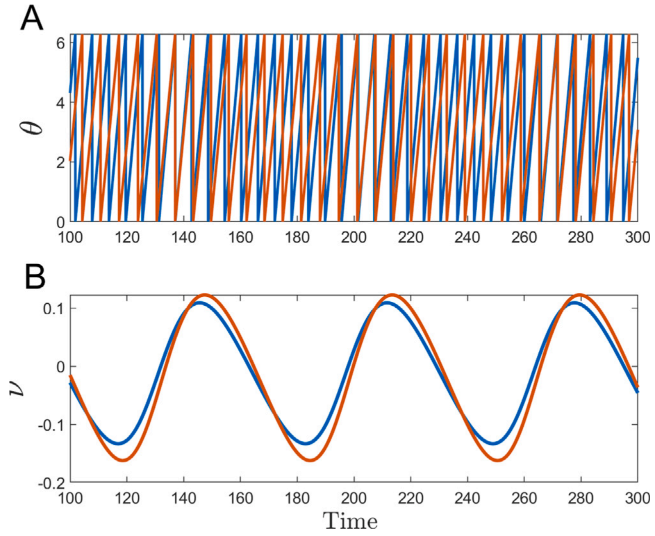

Fig. 8. The phase and amplitude dynamics of the phase–amplitude model. Panel A presents the phase dynamics of the first oscillator in blue and the second oscillator in red. Panel B presents the amplitude dynamics of the first oscillator in blue and the second oscillator in red.

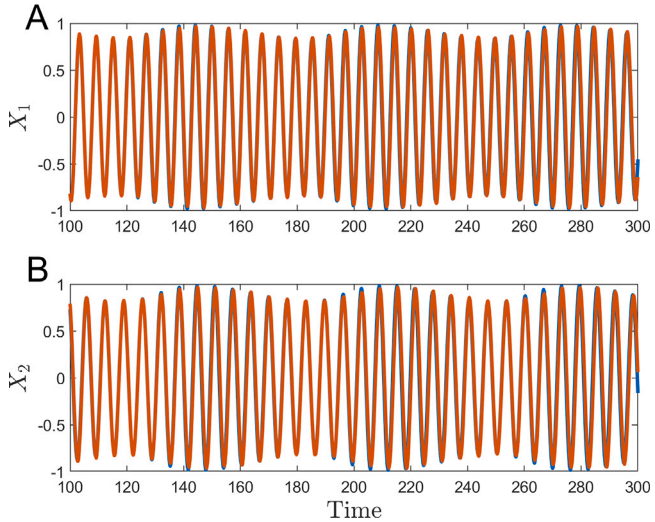

Fig. 9. This figure compares the full order model with dynamics defined in Eq. (27) to the inferred state from the phase–amplitude model with dynamics defined in Eq. (19). Panel A compares the dynamics of the X_1 variable in the full order model and phase–amplitude model. Panel B compares the dynamics of the X_2 variable in the full order model and phase–amplitude model. In both panels, the state in the full order model is plotted in blue and the comparable state derived from the phase-based model is shown in red. In each panel, the curves are nearly indistinguishable.

9. In this comparison, we have mapped the phase-based model back to its comparable state in the full order model using the relationship $X(\theta(t),\nu(t)) = X^{\gamma}(\theta(t)) + \nu(t)g(\theta(t))$. Recall that this is of the form defined in (7).

For further validation of the data-driven phase–amplitude model, we also compare the data-driven phase coupling function found using Eq. (17) to the actual phase coupling function computed analytically from the equations governing the system's dynamics. For our analytical calculation, we computed the phase response curves for each oscillator numerically using methods described in [8], and then calculated the coupling function according to

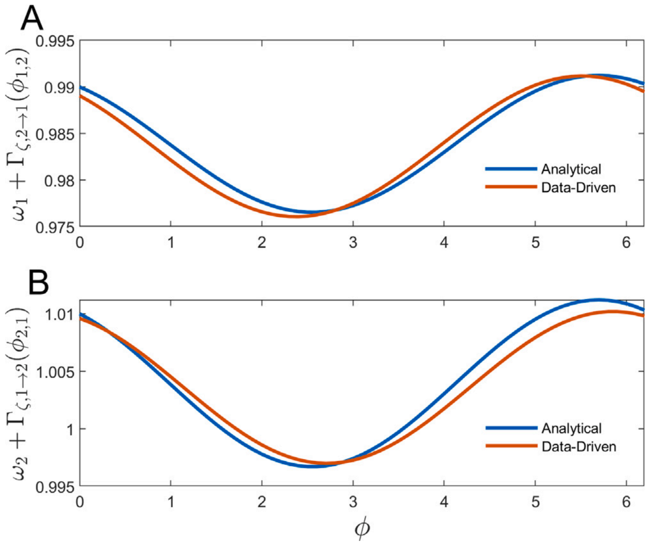

Fig. 10. This figure compares the numerically computed coupling functions defined in Eq. (28) to the data-driven coupling functions defined in Eq. (17) for a pair of coupled oscillators. Panel A presents this comparison for the first oscillator and panel B presents the comparison for the second oscillator.

$$\Gamma_{\zeta,k\to i}(\phi_{i,k}) = -\beta \frac{1}{T_0}\int_0^{T_0} Z_i(\zeta_i+\omega_0 t)\Big(X_i(\zeta_i+\omega_0 t) - X_j(\zeta_i+\omega_0 t-\phi_{i,j})\Big)dt. \tag{28}$$

Here, $\omega_0 = 2\pi/T_0$ and T_0 is the average period of the two oscillators. For this comparison, we reduced the heterogeneity so that the natural frequencies of the coupled oscillators were $C_1 = \omega_1 = 0.99$ and $C_2 = \omega_2 = 1.01$. We also decreased the coupling strength to $\beta = 0.008$. This ensured that the timescales of the terms in the averaged equations were close. Low heterogeneity is not necessary for the application of our algorithm, but was used here to compute the analytical coupling functions between oscillators with varying timescales for direct comparison to the numerical coupling functions computed using our algorithm. These results are presented in Fig. 10 where the coupling functions are plotted over the phase difference ϕ. The coupling functions for the first oscillator are shown in panel A, and the coupling functions for the second oscillator are shown in panel B.

5. Neural population-level oscillations

One motivation for this work is the possible application of this data-driven technique to coupled neural subnetworks. The existence of population-level neural dynamics has been studied since the electroencephalogram (EEG) first recorded electrical activity in the brain [43, 44]. Since then, numerous researchers have investigated these population-level dynamics to uncover their reasons and functions [45–49]. Recent research has also considered population-level oscillations in computational neural models [50].

The conductance-based neural model used in this work has voltage dynamics

$$\frac{\dot V_i}{C} = I_{b_i} - I_L(V_i) - I_{Na}(V_i,h_i) - I_K(V_i,h_i) - I_T(V_i,r_i) + I_{c_i} + \sqrt{2D}\eta_i(t), \tag{29}$$

$$i = 1,\dots,N,$$

where V_i is the transmembrane voltage of neuron i, I_{b_i} is a baseline stimulus, I_L, I_{Na}, I_K and I_T are ionic currents, I_{c_i} is the current due

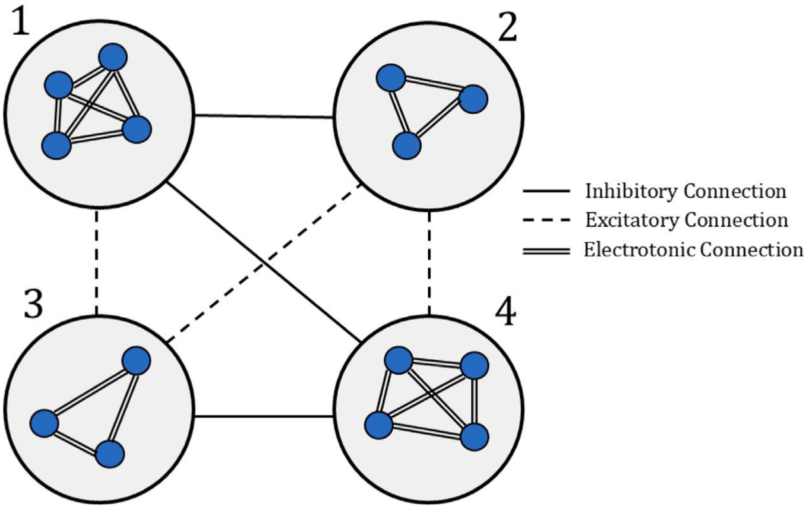

Fig. 11. A network containing four neuronal subnetworks. Neurons within each subnetwork are interconnected with electrotonic coupling. Neurons in different subnetworks are coupled with inhibitory or excitatory synaptic coupling.

to coupling, h_i, and r_i are gating variables, and $\sqrt{2D}\eta_i$ is a white noise process that is independent for each neuron. A full explanation of additional variables and parameters can be found in Appendix. In a data-driven setting the underlying dynamics and coupling structure of the individual oscillators are unknown. Instead, we assume that the only measured observable we can obtain from the system is the average voltage of each subnetwork

$$\bar{V}_m = \frac{1}{N_m}\sum_{i=1}^{N_m} V_i, \tag{30}$$

where N_m is the number of neurons in the mth subnetwork.

In the examples that follow, we consider a prototype model of coupled neurons organized into various subnetworks. This specific prototype possesses features of neuronal networks, but is not modeled on a specific brain circuit. An illustration of this prototype model is presented in Fig. 11 for a network of four subnetworks. Each subnetwork contains a population of neurons whose coupling structure reflects the coupling defined in Eq. (A.4). The neurons within each subnetwork are coupled with electrotonic coupling. Coupling between neurons in different subnetworks is inhibitory or excitatory synaptic coupling. The electrotonic coupling between neurons within the same subnetwork exerts a stronger force than the synaptic coupling between neurons in different subnetworks.

We assume that each subnetwork has a population-level limit cycle. The following two sections will discuss the application of our data-driven technique on neuronal networks of two and four subnetworks.

6. A neuronal network of two subnetworks

First we considered a two subnetwork system of $N = 1000$ neurons with dynamics defined in Eq. (A.1) and related equations in Appendix. A complete description of the parameters in this model can also be found in Section A.1 of Appendix. Below, we present our methodology and results following the steps given in Section 3.2.

6.1. Fitting the model to data

To begin, we evaluated this system for 2000 ms and obtained voltage dynamics for all $N = 1000$ neural oscillators. We then calculated the average voltage of the oscillators in each subnetwork $\bar{V}_m$ using Eq. (30). The voltages for the neurons in each subnetwork are presented in Fig. 12 for a 200 ms snapshot, with panel A plotting the voltages in the first subnetwork and panel B plotting the voltages in the second. The average voltage of each subnetwork as defined in Eq. (30) is overlayed in black on the respective panel, demonstrating the existence of population-level oscillations.

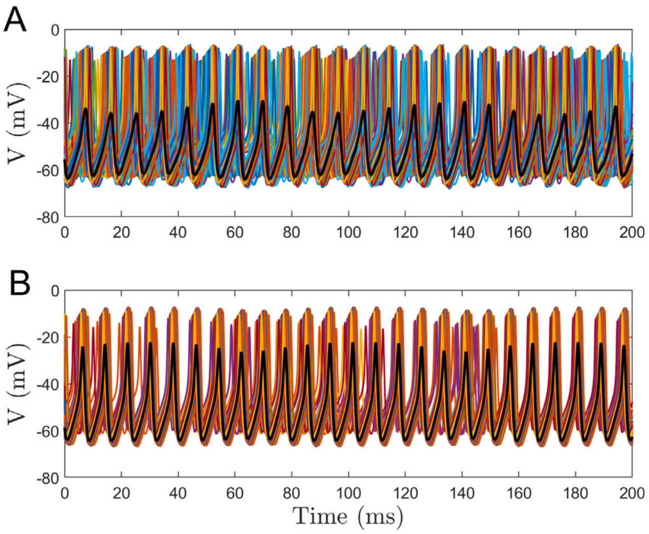

Fig. 12. Voltage dynamics of all neurons in a two subnetwork system. Panel A presents the voltages for the first subnetwork, and panel B presents the voltages for the second subnetwork. The black trace on each panel represents the average voltage of the given subnetwork which is taken as the observable for this system.

Our proposed strategy is implemented using the average voltage of each subnetwork as the observable. We define the $\theta = 0$ isochron to be when $\bar{V}_1 = -51.3$ mV with $\dot{\bar{V}}_1 > 0$ for the first subnetwork and $\bar{V}_2 = -50.7$ mV with $\dot{\bar{V}}_2 > 0$ for the second subnetwork. These values are equivalent to the mean values of $\bar{V}$ for each subnetwork. We then extracted the average voltage dynamics between subsequent crossings of the $\theta = 0$ isochron for each subnetwork. We have plotted these cycles in Fig. 13, with panel A showing the information for the first subnetwork, and panel B showing the information for the second subnetwork. Note that these cycles are plotted over time so that we can visually see the variation in both the amplitude of the oscillations as well as the time between isochron crossings.

From the data in Fig. 13, we found discrete approximations of $\dot{\theta}_i$, $\dot{v}_i$, v_i and $\phi_{i,j}$ and defined A_1, B_1, A_2, and B_2 following Steps 4–10

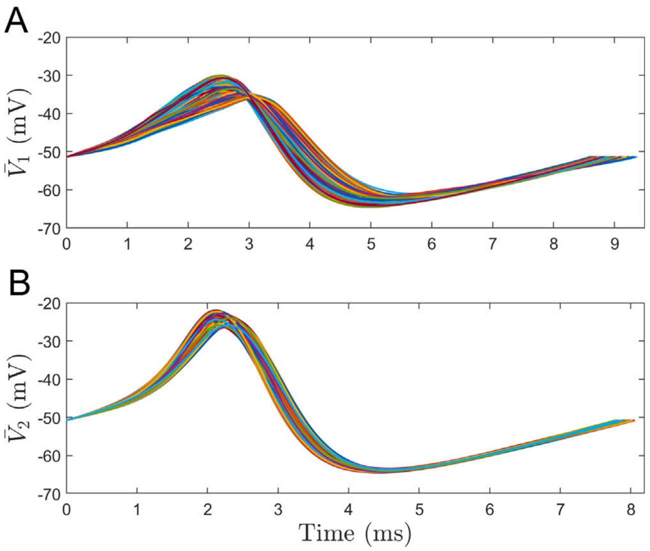

Fig. 13. Voltage dynamics between $\theta = 0$ isochron crossings for each subnetwork. Panel A presents the dynamics for the first subnetwork, and panel B presents the dynamics for the second subnetwork.

of Section 3.2. In this application, we chose the amplitude coordinate of the ith oscillator to be $v_k^i = \max(\bar{V}_k^i) - \min(\bar{V}_k^i) - v_{0,i}$, where $v_{0,i} = \frac{1}{N_{cross}-1}\sum_{k=1}^{N_{cross}-1}\left(\max(\bar{V}_k^i) - \min(\bar{V}_k^i)\right)$ for each kth crossing of the $\theta = 0$ isochron. With the B_1 vector and A_1 matrix, we evaluated Eq. (25) and determined the Fourier series coefficients that govern the phase dynamics. With the B_2 vector and A_2 matrix, we then evaluated Eq. (26) and determined the Fourier series coefficients that govern the amplitude dynamics. The F_1 and F_2 vectors contain the Fourier series coefficients that are used in the reduced order model defined in Eq. (19). In this example, we used a second-order Fourier series approximation.

In Fig. 14, we present a direct comparison between measured observables $B_1 \approx \dot{\theta}_i(t_k)$ as defined in Eq. (23) and the evaluation of $A_1 F_1$ from Eq. (25). Similarly, Fig. 15 presents a comparison between the measured observables $B_2 \approx \dot{v}_i(t_k)$ from Eq. (24) and the evaluation of $A_2 F_2$ from Eq. (26). These are plotted over the range of phase differences used in the terms of the A_1 and A_2 matrices in Eqs. (21) and (22), In both figures, the observable data $\dot{\theta}_i$ and $\dot{v}_i$ is shown in blue and the approximations using $A_1 F_1$ and $A_2 F_2$ are in black. In both figures, panel A presents this information for the first subnetwork and panel B presents this information for the second subnetwork.

6.2. Comparisons between ground truth and inferred model simulations

Finally, to test the model, we simulated the reduced-order model defined in Eq. (19) using the Fourier series coefficients found with Eqs. (25) and (26). The phase and amplitude coordinates from this simulation are shown in Fig. 16 for a 200 ms snapshot.

We compare the ground truth model with the reduced order model by approximating identical initial conditions of the full order model in the phase space and evolving the reduced order model forward in time. We present a comparison of the two simulations in Fig. 17. For this comparison, we have mapped the reduced order model back to its comparable state in the full order model using the relationship $\bar{V}\left(\theta(t), v(t)\right) = \bar{V}^{\gamma}\left(\theta(t)\right) + v(t)g\left(\theta(t)\right)$ as defined in (7).

For additional validation of the data-driven reduced order model, we also present Fig. 18 which plots the normalized count of voltage values for each subnetwork in both the full and reduced order models. Along with this, we also computed the mean μ_{ISI} and the variance var_{ISI} of the interspike intervals for each subnetwork in both the full and reduced order models. In the first subnetwork, $\mu_{ISI} = 8.88$ ms and $var_{ISI} = 3.6\text{e}{-2}$ for the full order model while $\mu_{ISI} = 8.88$ ms and $var_{ISI} = 3.0\text{e}{-2}$ for the reduced order model. In the second subnetwork, $\mu_{ISI} = 7.93$ ms and $var_{ISI} = 6.9\text{e}{-3}$ for the full order model while $\mu_{ISI} = 7.93$ ms and $var_{ISI} = 6.4\text{e}{-3}$ for the reduced order model. Fig. 18 along with the additional statistics support the visual

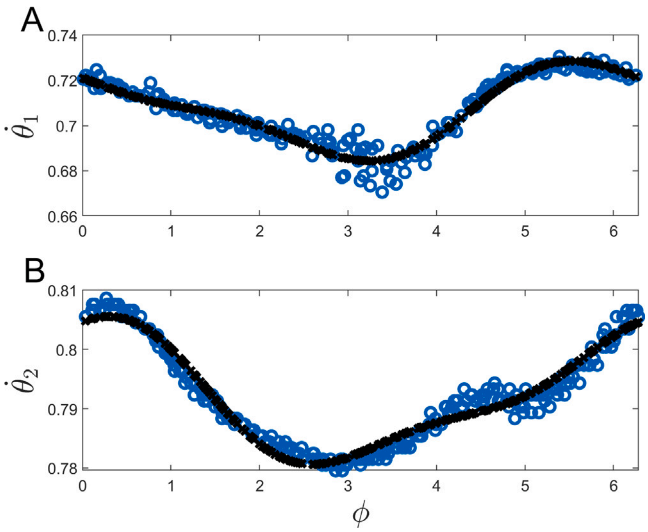

Fig. 14. This figure validates the least-squares approximation of the Fourier series coefficients for the phase dynamics derived in Section 3.2 for this network of two subnetworks. It directly compares the measured data defined in Eq. (23) with the evaluation of $A_1 F_1$, where A_1 and F_1 are calculated using the steps in Section 3.2. These are plotted as a function of the phase difference ϕ calculated in Step 8 of Section 3.2 and found in the terms of the A_1 matrix. The measured data from Eq. (23) is shown in blue and the data from the evaluation of $A_1 F_1$ is shown in black. Panel A presents the results for the first subnetwork and panel B presents the results for the second subnetwork.

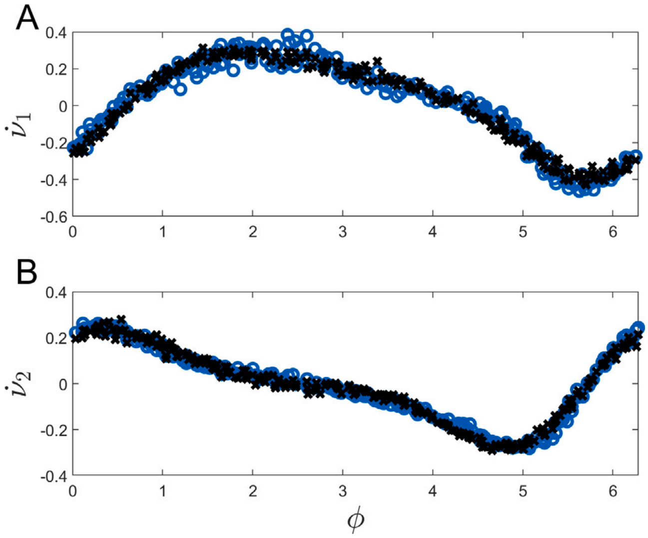

Fig. 15. This figure validates the least-squares approximation for the amplitude dynamics derived in Section 3.2 for this network of two subnetworks. It directly compares the measured data defined in Eq. (24) with the evaluation of $A_2 F_2$, where A_2 and F_2 are calculated following the steps in Section 3.2. These are plotted as a function of the phase difference ϕ calculated in Step 8 of Section 3.2 and found in the terms of the A_2 matrix. The measured data from Eq. (24) is shown in blue and the data from the evaluation of $A_2 F_2$ is shown in black. Panel A presents the results for the first subnetwork and panel B presents the results for the second subnetwork.

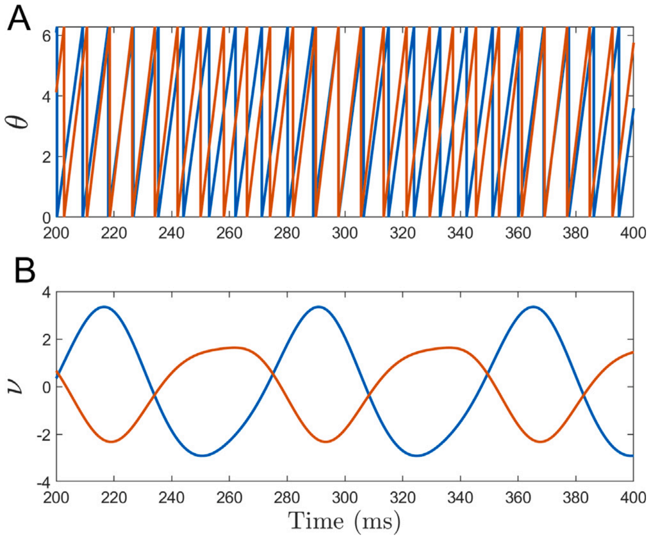

Fig. 16. The phase and amplitude dynamics of the reduced order model. Panel A presents the phase dynamics of the first subnetwork in blue and the second subnetwork in red. Panel B presents the amplitude dynamics of the first subnetwork in blue and the second subnetwork in red.

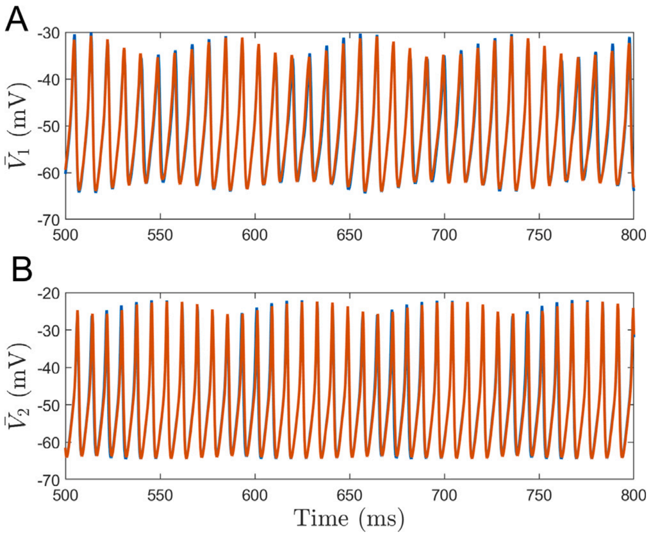

Fig. 17. This figure compares the full order model with dynamics defined in Eqs. (A.1)–(A.5) in Appendix to the comparable states inferred from the reduced order model defined in Eq. (19). Panel A (resp., B) compares the dynamics of $\bar{V}_1$ (resp., $\bar{V}_2$) in the full and reduced order models. In both panels, the state in the full order model is plotted in blue and the comparable state derived from the reduced order model is shown in red. In each panel, the curves are again almost indistinguishable.

results presented in Fig. 17, demonstrating that the data-driven reduced order model yields a close approximation to the full order model.

Finally, to clearly demonstrate the importance of coupling in the evaluation of our system's phase response curves (PRCs), we present Fig. 19. In this figure, a series of phase response curves are computed numerically using variations of the direct method. In the direct method, a series of perturbations applied to the full order model are used to find an approximate phase response curve $Z(\theta)$. Each plot in Fig. 19 is a single phase response curve obtained from a sample of 40 different perturbations. In blue, we compute phase response curves that account for coupling, while in red we do not account for coupling.

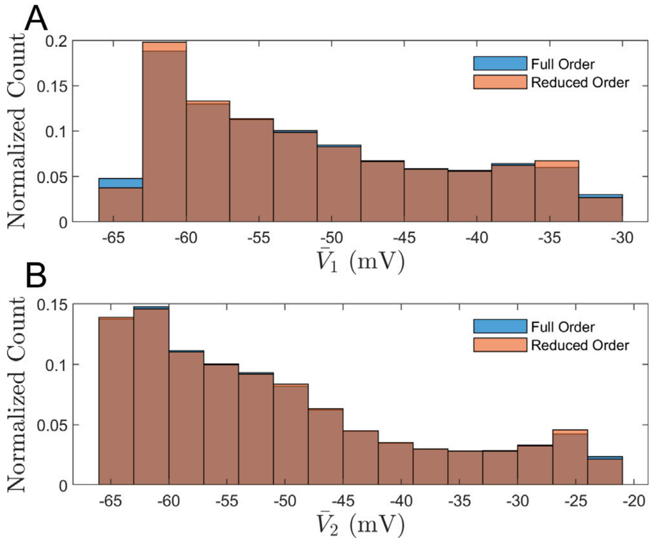

Fig. 18. This figure presents the normalized count of $\bar{V}$ values for the full and reduced order model. Panel A presents this data for the first subnetwork. Panel B presents this data for the second subnetwork.

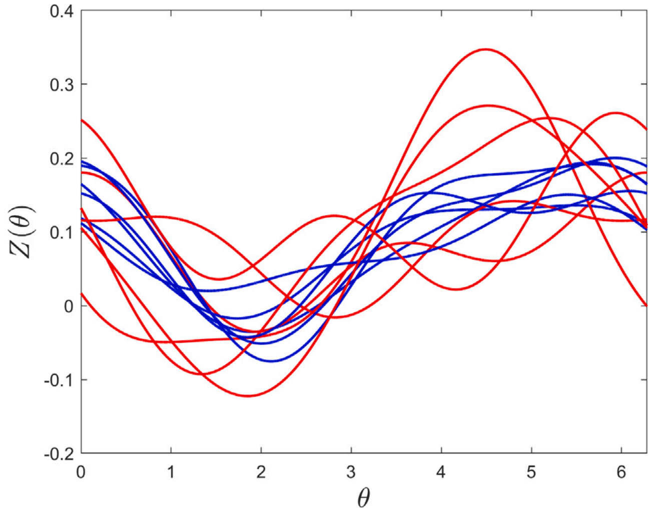

Fig. 19. Various numerical approximations of a single subnetwork's phase response curve using the direct method. The curves in blue incorporate coupling in the computation of the numerical PRCs while the curves in red do not incorporate coupling.

To begin the numerical computation of these PRCs, we first simulated the full order model defined in Eq. (A.1) and applied a series of perturbations to all neurons in a single subnetwork. Since the average voltage of the subnetwork $\bar{V}$ is known at the time of perturbation t_p, the phase θ can be inferred.

To find pointwise approximations of $Z(\theta)$ at each phase θ, we will use the equation $Z(\theta) \approx d\theta/(u\Delta t_p)$. Here, u is the applied magnitude of the perturbation, Δt_p is the duration that the perturbation is applied, and $d\theta$ is the resulting phase difference between the perturbed and unperturbed system. The calculation of $d\theta$ is done 2–3 cycles after the time of perturbation at some time t_m. The value of $d\theta$ is obtained by comparing the phase inferred from measured data to the phase from unperturbed simulations of the reduced order model. In Fig. 19, the phase response curves in blue are found by calculating the unperturbed phase with the reduced order model defined in (19). Conversely, the phase response curves in red ignore the Fourier series terms that account for coupling in Eq. (19) in the computation of the unperturbed phase. The

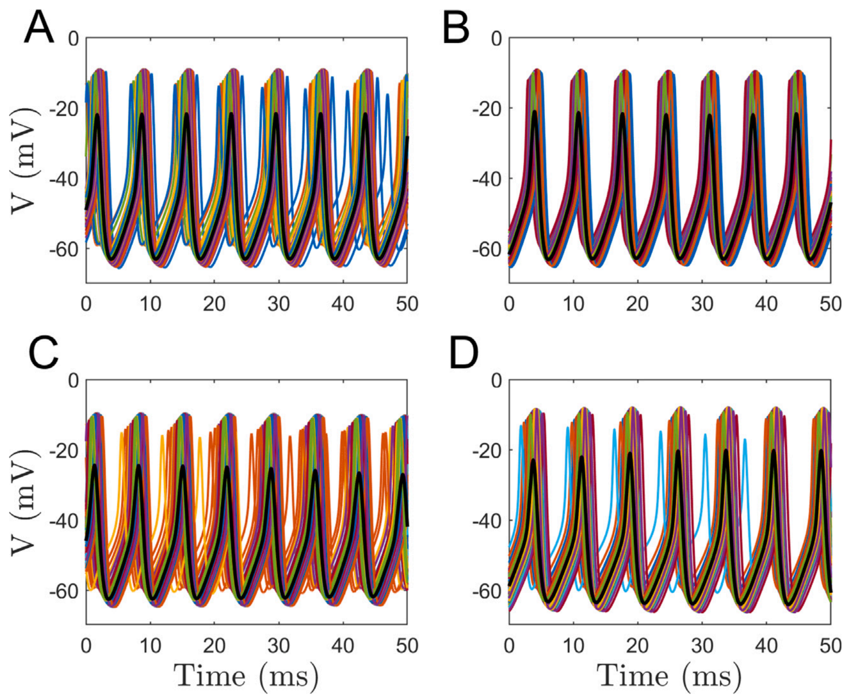

Fig. 20. Voltage dynamics for all neurons in a four subnetwork system. Panels A-D present the voltages for subnetworks 1–4, respectively. A black trace on each panel represents the average voltage of that subnetwork. These average voltages are the observables for this system.

resulting pointwise estimates are fit using the lowest harmonics of a Fourier basis to obtain the phase response curve.

Without incorporating coupling, the red PRCs appear noisy with no discernible average curve. However, the blue plots evaluated using Eq. (19) and incorporating coupling appear much more consistent and follow a discernible curve. Using a larger number of perturbations to compute the phase response curves would yield more accurate approximations to the actual phase response curve.

7. A neuronal network of four subnetworks

Finally we considered a four subnetwork system of $N = 1000$ neurons with dynamics defined in Eq. (A.1) and related equations in Appendix. A complete description of the parameters of this model can be found in Section A.2 of Appendix. We present our methodology and results in chronological order following the steps given in Section 3.2 below.

7.1. Fitting the model to data

We evaluated this system for 2000 ms and obtained voltage dynamics for all $N = 1000$ neural oscillators. We calculated the average voltage of the oscillators in each subnetwork $\bar{V}_m$ using Eq. (30). The voltages for the neurons in each subnetwork are presented in Fig. 20 for a 50 ms snapshot, with panels A-D plotting the voltages in subnetworks 1–4, respectively. The average voltage of each subnetwork as defined in Eq. (30) is overlayed in black on the respective panels, clearly demonstrating the existence of population-level oscillations.

Our proposed strategy is implemented using the average voltage of each subnetwork as the observable. We define the $\theta = 0$ isochron to be when $\bar{V}_1 = -50.0$ mV and $\dot{\bar{V}}_1 > 0$ for the first subnetwork, $\bar{V}_2 = -50.1$ mV and $\dot{\bar{V}}_2 > 0$ for the second subnetwork, $\bar{V}_3 = -50.0$ mV and $\dot{\bar{V}}_3 > 0$ for the third subnetwork, and $\bar{V}_4 = -50.1$ and $\dot{\bar{V}}_4 > 0$ for the fourth subnetwork. These values are equivalent to the mean values of $\bar{V}$ for each subnetwork. We extracted the average voltage between subsequent crossings of the $\theta = 0$ isochron for each subnetwork. These cycles are plotted in Fig. 21, with panels A-D showing the information for subnetworks 1–4 respectively. These cycles are plotted over time so that we can visually identify variation in the amplitude of the oscillations as well as the time between isochron crossings.

Using the data in Fig. 21, we found discrete approximations of $\dot{\theta}_i$, $\dot{v}_i$, v_i and $\phi_{i,j}$ and defined A_1, B_1, A_2, and B_2 following Steps 4–10 of Section 3.2. In this application, we defined the amplitude coordinate of the ith oscillator to be $v_k^i = \max(\bar{V}_k^i) - \min(\bar{V}_k^i) - v_{0,i}$ where $v_{0,i} = \frac{1}{N_{cross}-1} \sum_{k=1}^{N_{cross}-1} \left(\max(\bar{V}_k^i) - \min(\bar{V}_k^i)\right)$. With the B_1 vector and A_1 matrix, we evaluated Eq. (25) and determined the Fourier series coefficients that govern the phase dynamics. With the B_2 vector and A_2 matrix, we evaluated Eq. (26) and determined the Fourier series coefficients that govern the amplitude dynamics. The F_1 and F_2 vectors contain the Fourier series coefficients that are used in the reduced order model defined in Eq. (19). For this example, we used a second-order Fourier series approximation.

7.2. Comparisons between ground truth and inferred model simulations

Finally, to test our method, we simulated the reduced order model defined in Eq. (19) with the Fourier series coefficients found using Eqs. (25) and (26). The amplitude coordinates obtained from this simulation are shown in Fig. 22 for a 200 ms snapshot.

We compare the ground truth model with the reduced order model by again approximating identical initial conditions of the full order model in the phase space and evolving the reduced order model defined in Eq. (19) forward in time. We present a comparison of the two simulations in Fig. 23. For this comparison, we have mapped the reduced order model back to its comparable state in the full order model using the relationship $\bar{V}\big(\theta(t), v(t)\big) = \bar{V}^{\gamma}\big(\theta(t)\big) + v(t) g\big(\theta(t)\big)$ as defined in Eq. (7).

For additional validation of the data-driven reduced order model in this application, we present Fig. 24, which plots the normalized count of voltage values for each subnetwork in both the full and reduced order models. Along with this, we also computed the mean and variance of the interspike intervals for each subnetwork in the full and reduced order models. For the first subnetwork, $\mu_{ISI} = 6.89$ ms and $var_{ISI} = 1.3\text{e}{-3}$ in the full order model, while $\mu_{ISI} = 6.89$ ms and

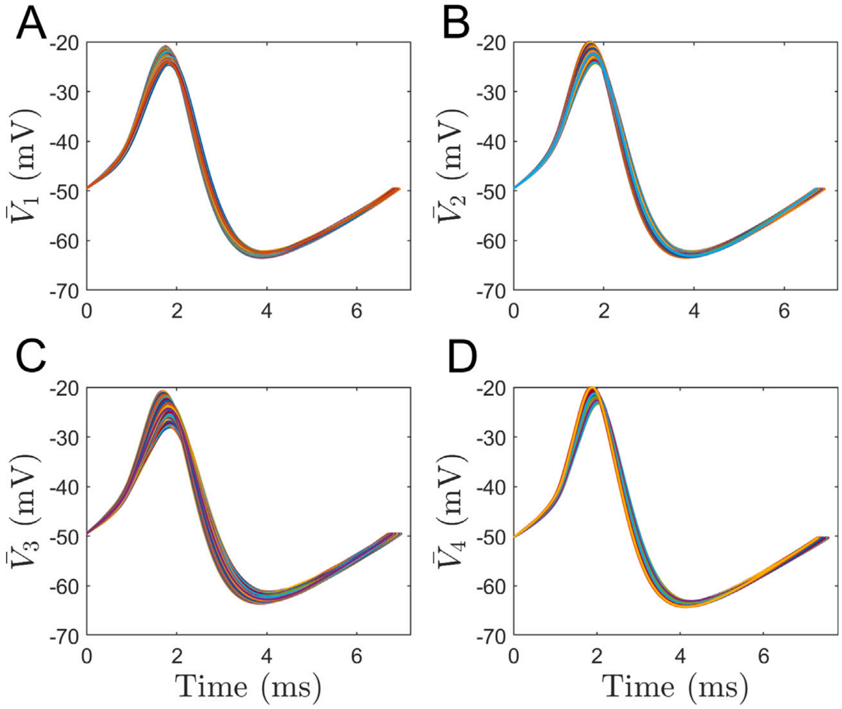

Fig. 21. Voltage dynamics between $\theta = 0$ isochron crossings for each subnetwork. Panels A-D present the dynamics for subnetworks 1–4, respectively.

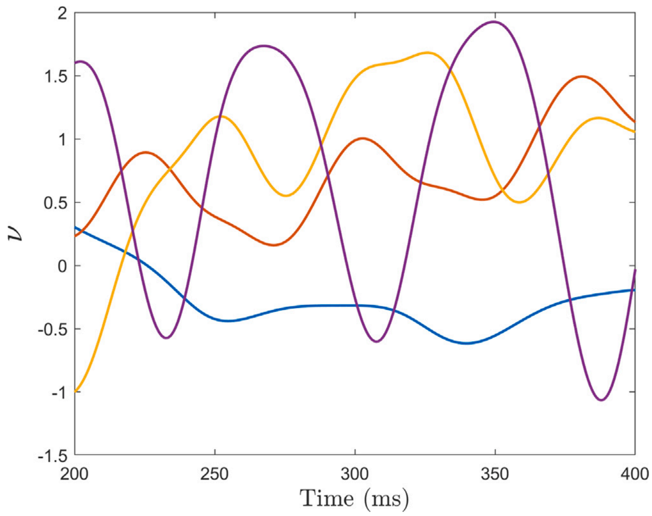

Fig. 22. The amplitude dynamics of the reduced order model for each of the four subnetworks.

var_{ISI} = 7.0e−4 in the reduced order model. In the second subnetwork, μ_{ISI} = 6.80 ms and var_{ISI} = 2.1e−3 for the full order model, while μ_{ISI} = 6.80 ms and var_{ISI} = 1.6e−3 for the reduced order model. In the third subnetwork, μ_{ISI} = 6.85 ms and var_{ISI} = 4.4e−3 for the full order model, while μ_{ISI} = 6.86 ms and var_{ISI} = 3.9e−3 for the reduced order model. Finally in the fourth subnetwork, μ_{ISI} = 7.42 ms and var_{ISI} = 4.5e−3 for the full order model, while μ_{ISI} = 6.43 ms and var_{ISI} = 3.3e−3 for the reduced order model. Fig. 24 along with the additional statistics regarding the interspike intervals support the visual results presented in Fig. 23, demonstrating again that the data-driven reduced order model yields a close approximation to the full order model. Note that with more subnetworks, the variances are not matched as close as they were in the previous example with only two subnetworks.

8. Limitations of this approach

In the previous two sections, the neural oscillators possess an all-to-all coupling structure. In addition, we assume that all neurons within each subnetwork can be observed so that the average voltage of each subnetwork ($\bar{V}$) is the true average voltage of the subpopulation. In this section, we will briefly explore some of the limitations of our proposed technique as it relates to these two properties. First, we will investigate the efficacy of this technique on neural populations where the coupling is less than all-to-all. Then we investigate the limitations of this algorithm in populations where only a subset of neurons is observable within each subnetwork.

8.1. Limitations due to coupling

The ability to effectively implement this technique on networks of subnetworks is predicated on the existence of population-level oscillations in each subnetwork. Due to this fact, its success is not dependent on the coupling structure of the network and it will work for arbitrary coupling provided: (1) the population-level oscillations do not approach a state near complete desynchronization (defined when $\bar{V} = 0$), and (2) approximations of $\dot{\theta}$ and $\dot{\nu}$ can be taken over the entire range of $\phi \in [0, 2\pi)$.

To specifically demonstrate that our method works with different coupling, Fig. 25 illustrates the application of our algorithm on a network of two subnetworks using the dynamics and parameters defined in Section 6 and Appendix A.1, but with reduced coupling. Instead of all-to-all coupling, 80% of the coupling connections are removed randomly. In panel A, we note that despite significantly reduced coupling, a single subnetwork still possesses strong population-level oscillations. This can be further viewed in panel B, which shows the cycles between isochron crossings for this subnetwork. In panel C, note that we still

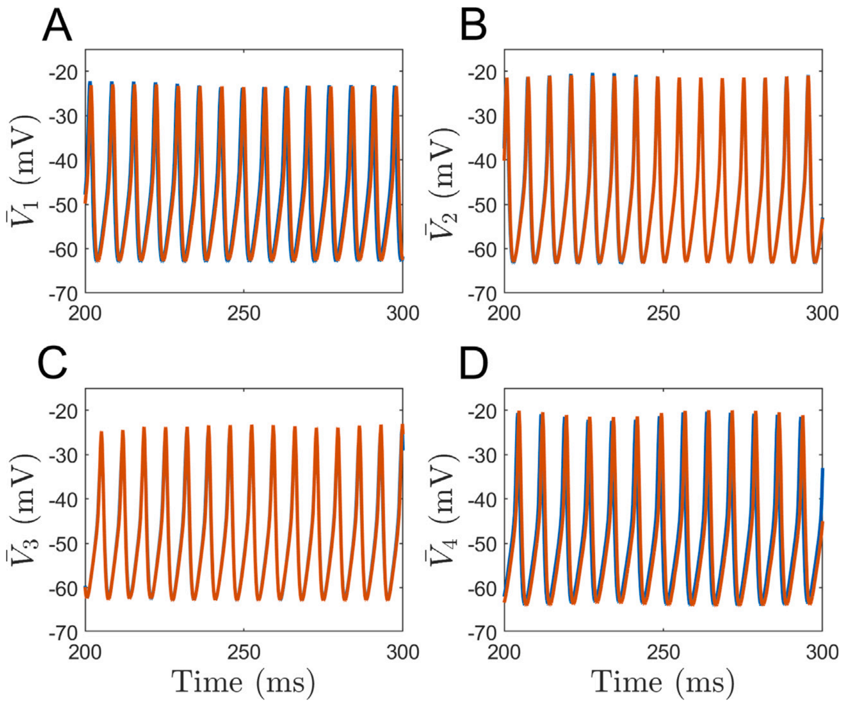

Fig. 23. This figure compares the full order model with dynamics defined in Eqs. (A.1)–(A.5) in Appendix to the comparable states inferred from the reduced order model defined in Eq. (19). Panels A-D compare the dynamics of $\bar{V}_1 - \bar{V}_4$ in the full order model and reduced order model. In all panels, the state in the full order model is plotted in blue and the comparable state derived from the reduced order model is shown in red. The curves match closely and are nearly indistinguishable in all panels.

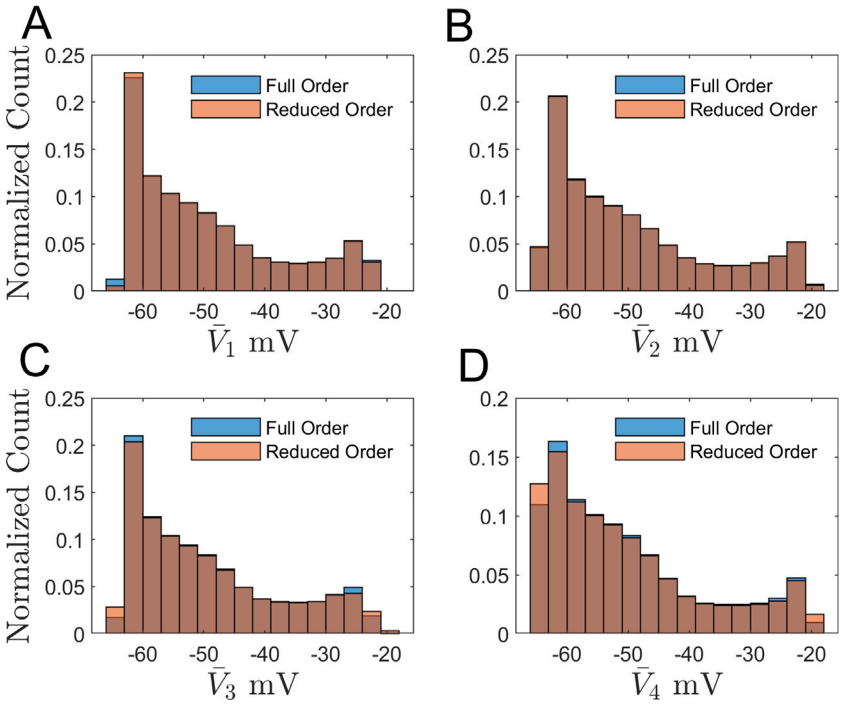

Fig. 24. This figure presents the normalized count of $\bar{V}$ for the full and reduced order model. Panels A-D present the data for subnetworks 1–4, respectively.

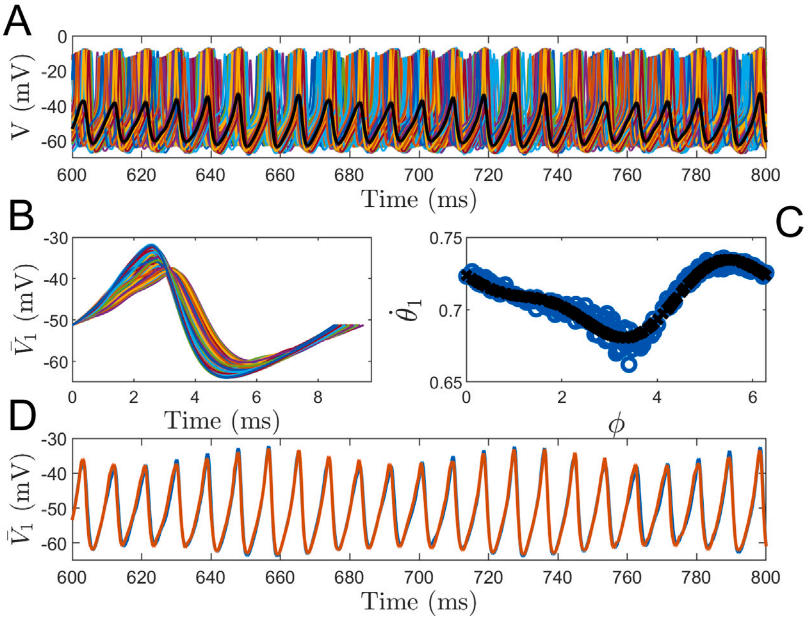

Fig. 25. This figure demonstrates the effective application of our algorithm on a two subnetwork system with the same dynamics and parameters defined in Section 6 and Appendix but with 80% of coupling connections removed randomly. Panel A plots all of the voltage traces contained in a single subnetwork with the black trace associated with the average voltage overlaid on top. The black trace clearly demonstrates the existence of population-level oscillations. Panel B presents each cycle of the average voltage between $\theta = 0$ isochron crossings, again demonstrating the existence of population level dynamics and showing variation in both the amplitudes and the times between successive $\theta = 0$ isochron crossings. In panel C, we compare the measured data defined in Eq. (23) with the evaluation of $A_1 F_1$, where A_1 and F_1 are calculated using the steps in Section 3.2. Panel D presents a comparison between the average voltage from the full order model (in blue) with the comparable state inferred from the reduced order model defined in Eq. (19).

obtain approximations of $\dot{\theta}$ across the range $\phi \in [0, 2\pi)$, and that our Fourier series representation yields a close approximation to the data. Finally, in panel D, we note that the inferred state from our reduced model closely matches the actual average voltage.

Our approach begins to break down after decreasing the coupling further by removing a total of 97% of coupling connections. The results from this trial can be seen in Fig. 26. There is significantly less agreement between the plots in panel D, which compares the actual voltage average and the inferred state from our reduced order simulation. Panels B and C demonstrate why this technique is losing its efficacy: in panel B, we see that some of the cycles between isochron crossings are approaching a desynchronized state, and in panel C, we notice that the datapoints for $\dot{\theta}$ vary more significantly at each phase difference ϕ so that the error in our least squares approximation is larger than in previous simulations.

Decreasing coupling further by removing a total of 99% of coupling connections, our population-level oscillations nearly disappear as we are close to the threshold of complete desynchronization of the neural population. The results from the application of our technique to this simulation can be found in Fig. 27. Panels A, B, and D demonstrate that we are close to desynchronization. In Panel C, we also notice that we do not have $\dot{\theta}$ data points over the entire range of possible phase differences (yet another complication). These reasons help explain why our method is insufficient at capturing the dynamics of this system in panel D.

The exact limits of this technique in regards to the coupling structure will vary on a per system basis and will depend on the coupling strength, the noise intensity, the heterogeneity of the network, and the incorporation of any additional subnetworks.

8.2. Limitations due to observable data

To investigate the effect of limited observability among our individual oscillators, we ran a series of simulations where the average voltage of each subnetwork was computed using only a subset of each population of neurons. This data was used to infer a reduced order model, and the results were directly compared to the true average voltage. For this example, we will utilize the two subnetwork, 1000 neuron network described in Section 6 and related equations in Appendix.

Moving forward, we will be using $\bar{V}$ to denote the true average voltage of a single subnetwork in the full order model and $\bar{V}^x$ to represent the average voltage inferred from a reduced order model, where x indicates the number of observed neurons in a given subnetwork. In the example below, the value of x as a percentage of the 500 total neurons in a single subnetwork is defined in the legend of panel A in Fig. 28. Panel A shows the root mean squared error (RMSE) as defined in Eq. (31) over N_{steps} total time steps. Note that the RMSE increases substantially when less than 10% of the neurons (50 neurons) are observed. Panel B of Fig. 28 shows $\bar{V}^x$ over time for the values of x indicated in the legend of panel A. Panel C plots $\bar{V} - \bar{V}^x$ over the same time span and for the same values of x shown in panel B. This figure demonstrates that our method does indeed accommodate limited observability in large populations of oscillators.

$$\text{RMSE} = \frac{\sum_{k=1}^{N_{steps}} (\bar{V}_k - \bar{V}_k^x)^2}{N_{steps}} \tag{31}$$

9. Discussion and conclusion

Phase-based model order reduction methods are frequently used to analyze high-dimensional, nonlinear dynamical systems that possess a stable limit cycle. Existing phase-based, data-driven model identification strategies assume the existence of a single, uncoupled limit cycle oscillator and cannot be straightforwardly implemented in applications where there are multiple coupled oscillators. In this work, we derive a data-driven phase–amplitude reduced order modeling technique for

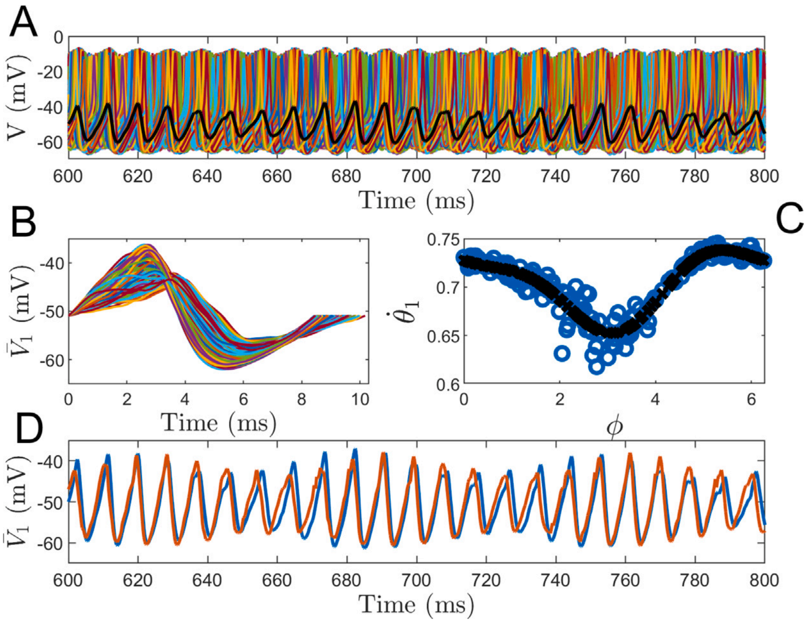

Fig. 26. This figure demonstrates the attempted application of our algorithm on a two subnetwork system with the same dynamics and parameters defined in Section 6 and Appendix but with 97% of the coupling connections removed randomly. Panel A plots all of the voltage traces contained in a single subnetwork with the black trace associated with the average voltage overlaid on top. The black trace still demonstrates the existence of population-level oscillations. Panel B presents each cycle of the average voltage between $\theta = 0$ isochron crossings, again demonstrating the existence of population level dynamics but clearly showing that our average voltage is at times much closer to the threshold of complete desynchronization. In panel C, we compare the measured data defined in Eq. (23) with the evaluation of $A_1 F_1$, where A_1 and F_1 are calculated using the steps in Section 3.2. Panel D presents a comparison between the average voltage from the full order model (in blue) with the comparable state inferred from the reduced order model defined in Eq. (19). Here we see much less agreement between the full and reduced order model.

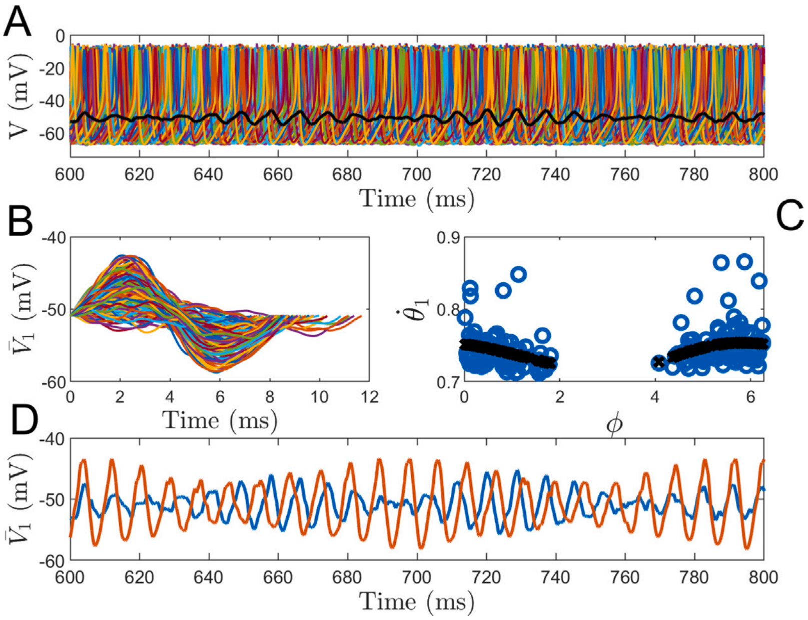

Fig. 27. This figure demonstrates the failed application of our algorithm on a two subnetwork system with the same dynamics and parameters defined in Section 6 and Appendix but with 99% of coupling connections removed randomly. Panel A plots all of the voltage traces contained in a single subnetwork with the black trace associated with the average voltage overlaid on top. There is no longer steady and discernible population-level oscillations. Panel B presents each cycle of the average voltage between $\theta = 0$ isochron crossings. In panel C, we compare the measured data defined in Eq. (23) with the evaluation of $A_1 F_1$, where A_1 and F_1 are calculated using the steps in Section 3.2. In this situation, we do not have any measured data in the range $\phi \in [2, 4]$, so we cannot obtain an accurate Fourier series representation of the dynamics. Panel D presents a comparison between the average voltage from the full order model (in blue) with the comparable state inferred from the reduced order model defined in Eq. (19). Here we see no agreement between the full and reduced order model.

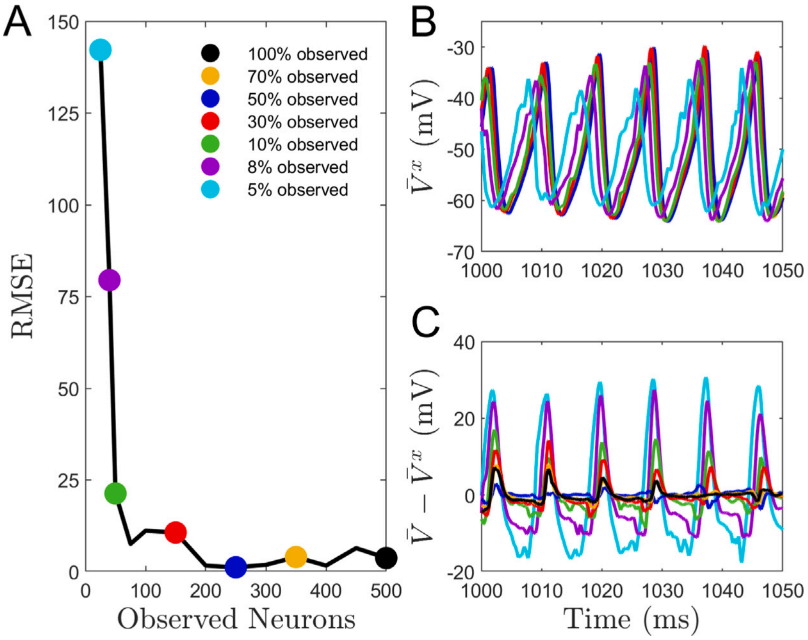

Fig. 28. This figure demonstrates that our proposed approach accommodates limitations in the observability of individual oscillators within a subpopulation. For these results, we simulated a 1000 neuron network comprised of two 500 neuron subnetworks with parameters and dynamics defined in Section 6 and Appendix A.1. Panel A plots the RMSE value for various $\bar{V}^x$ as calculated in Eq. (31). Panel B plots the voltage traces of $\bar{V}^x$. Panel C plots the difference between $\bar{V}^x$ and $\bar{V}$.

a system of coupled limit cycle oscillators. We apply this technique in three examples: (1) a two oscillator model of the nonradial isochron clock with coupling; (2) a two subnetwork, 1000 neuron system with electrotonic and synaptic coupling; and (3) a four subnetwork, 1000 neuron system with electrotonic and synaptic coupling. Our results demonstrate that the reduced order model is a close match to the full order model for all three examples. We also demonstrate the similarity between the analytical coupling functions for our systems, and their numerical least-squares approximations and investigate limitations with respect to coupling structure and observability of the networks.

The data-driven reduced order modeling technique implemented here incorporates the temporal dynamics intrinsic to the evaluated dynamical systems — specifically, the existence of stable limit cycles. Coupled limit cycle oscillators can be modeled with the modeling techniques described in this work if: (1) the underlying dynamical systems possess stable limit cycles; (2) the effects due to coupling, noise, and heterogeneity are relatively minimal with respect to the stable limit cycle; and (3) measurements of the phase and amplitude coordinates can be taken over the entire range of possible phase differences.

Some of the specific limitations we encountered relate to the coupling strength between limit cycle oscillators. Specifically, if the coupling strength was too strong, the oscillators possessed either strong synchronizing or antiphase tendencies. This made it impossible to derive a reduced-order model using this technique since ϕ did not generally extend over the entire range $[0, 2\pi]$ (related to point 3 in the previous paragraph). In the analysis of population-level oscillations, if the coupling strength within a subpopulation was too weak to produce discernible and steady population-level oscillations, our technique failed to yield an accurate reduced order model. Additionally, as we added more oscillators (or subnetworks), our accuracy degraded due to the high quantity of Fourier series terms that needed to be fit to the phase dynamics.

The model reduction strategies described in this paper are an adaptation of existing reduced order modeling techniques that consider a realistic scenario: a dynamical system whose structure and dynamics are mathematically unknown. In the future, we will consider extending these results by deriving the phase response curves and isostable response curves of more complicated networks of subnetworks (i.e., a 4 subnetwork system). Additionally, we will investigate the potential application of this technique to a system whose physical connections are unknown — that is, a system where we do not already know which neurons exist in the same subnetwork. We will consider extending our results to model control inputs using the reduced-order model.

CRediT authorship contribution statement

Kaitlyn Toth: Writing – original draft, Visualization, Validation, Methodology, Investigation, Formal analysis, Conceptualization. **Dan Wilson:** Writing – review & editing, Supervision, Resources, Project administration, Funding acquisition, Conceptualization.

Declaration of competing interest

The authors declare the following financial interests/personal relationships which may be considered as potential competing interests: Dan Wilson reports financial support was provided by National Science Foundation. Kaitlyn Toth reports financial support was provided by National Science Foundation.

Acknowledgment

This material is based upon the work supported by the National Science Foundation (NSF) under Grant No. CMMI-2140527.

Appendix. Neural model equations

A single conductance-based thalamic neuron in the network model considered in this work has dynamics from [51].

$$\frac{\dot{V}_i}{C} = I_{b_i} - I_L(V_i) - I_{Na}(V_i, h_i) - I_K(V_i, h_i) - I_T(V_i, r_i) + I_{c_i} + \sqrt{2D}\eta_i(t), \tag{A.1}$$

$$\begin{aligned} \dot{h}_i &= \left(h_\infty(V_i) - h_i\right)/\tau_h, \\ \dot{r}_i &= \left(r_\infty(V_i) - r_i\right)/\tau_r, \\ i &= 1, \dots, N, \end{aligned}$$

where V_i is the transmembrane voltage of neuron i, $C = 1$ μF/cm^2 is the constant membrane capacitance; $N = 1000$ is the total number of neurons in the network of subnetworks; I_{b_i} is an external baseline stimulus; I_{c_i} is the current due to coupling; I_L, I_{Na}, I_K, and I_T are the leak, sodium, potassium, and low-threshold calcium ionic currents; $\eta_i(t)$ is a zero-mean white noise process with intensity D; and h_i and r_i are gating variables. Additional equations that define this model are:

$$\begin{aligned} I_L(V_i) &= g_L(V_i - E_L), \\ I_{Na}(V_i, h_i) &= g_{Na}\left(m_\infty^3(V_i)\right)h_i(V_i - E_{Na}), \\ I_K(V_i, h_i) &= g_K\left(0.75(1 - h_i)^4\right)(V_i - E_K), \\ I_T(V_i, r_i) &= g_T\left(p_\infty^2(V_i)\right)r_i(V_i - E_T). \end{aligned} \tag{A.2}$$

$$\begin{aligned} h_\infty(V_i) &= 1/(1 + \exp((V_i + 41)/4)), \\ r_\infty(V_i) &= 1/(1 + \exp((V_i + 84)/4)), \\ \alpha_h(V_i) &= 0.128\exp(-(V_i + 46)/18), \\ \beta_h(V_i) &= 4/(1 + \exp(-(V_i + 23)/5)), \\ \tau_h(V_i) &= 1/(\alpha_h + \beta_h), \\ \tau_r(V_i) &= 28 + \exp(-(V_i + 25)/10.5), \\ m_\infty(V_i) &= 1/(1 + \exp(-(V_i + 37)/7)), \\ p_\infty(V_i) &= 1/(1 + \exp(-(V_i + 60)/6.2)). \end{aligned} \tag{A.3}$$

In Eq. (A.2), $g_L = 0.05$ mS/cm^2, $E_L = -70$ mV, $g_{Na} = 3$ mS/cm^2, $E_{Na} = 50$ mV, $g_K = 5$ mS/cm^2, $E_K = -90$ mV, $g_T = 5$ mS/cm^2, and $E_T = 0$ mV. Neuron i is coupled with electrotonic coupling to all neurons within the same subnetwork as neuron i and with synaptic coupling to all other neurons not in the same subnetwork as neuron i. The current due to coupling I_{c_i} is

$$I_{c_i} = \frac{1}{N-1}\Bigg[\underbrace{\sum_{j \neq i} K_{j\to i}(V_j - V_i)}_{\text{Electrotonic Current, Same Subnetwork}} - \underbrace{\sum_{j \neq i} g_{j\to i}s_j\left(V_i - E_{syn}(j,i)\right)}_{\text{Synaptic Current, Other Subnetworks}}\Bigg], \tag{A.4}$$

where $g_{j\to i}$ is the synaptic coupling strength between neurons i and j, $K_{j\to i}$ is the electrotonic coupling strength between neurons i and j, $E_{syn}(j,i)$ (in mV) is the synaptic reversal potential associated with the relevant synaptic current, and s_j is the synaptic variable with associated temporal dynamics

$$\dot{s}_i = \frac{c_1(1 - s_i)}{1 + \exp(-(V_i - V_T)/\sigma_T)} - c_2 s_i. \tag{A.5}$$

The synaptic variable has parameters $c_1 = 3$ (unitless), $c_2 = 1$ (unitless), $V_T = -20$ mV, and $\sigma_T = 0.8$ mV. The synaptic coupling strength $g_{j\to i}$, the synaptic reversal potential $E_{syn}(j,i)$, and the electrotonic coupling strength $K_{j\to i}$ are dependent on the subnetworks containing neurons i and j. For specific details regarding the parameters used in Sections 6 and 7 of this work, see the subsections below.

A.1. Parameters for the neuronal network of two subnetworks

For the two subnetwork system in Section 6, $N = 1000$ neurons with 500 neurons in each subnetwork. Both subnetworks are heterogeneous, with baseline stimuli $I_{b_i} \in [4.5, 4.7]$ μA/cm^2 for the first subnetwork and $I_{b_i} \in [5.5, 5.7]$ μA/cm^2 for the second subnetwork, both drawn from a uniform distribution. The noise intensity is $D = 0.0015$. The synaptic reversal potential $E_{syn} = -100$ mV for all synaptic connections in this example.

Table A.1
Table of synaptic coupling strengths between the two 500 neuron subnetworks analyzed in Section 6.

	$1 \le i \le 500$	$500 < i \le 1000$
$1 \le j \le 500$	0	0.0501
$500 < j \le 1000$	0.0501	0

Table A.2
Table of electrotonic coupling strengths, $K_{j\to i}$, between any two neurons i and j within the same subnetwork for the two 500 neuron subnetworks analyzed in Section 6.

	$1 \le i \le 500$	$500 < i \le 1000$
$1 \le j \le 500$	0.1501	0
$500 < j \le 1000$	0	0.1782

The synaptic coupling strength between any two neurons, i and j will depend on the subnetworks containing the neurons i and j. Table A.1 lists the synaptic coupling strength between neurons in the two subnetworks analyzed in Section 6. This value was chosen from a uniform distribution that spanned the range $[0.05, 0.1]$.

The electrotonic coupling strength between any two neurons i and j is the same for all neurons within that subnetwork. Table A.2 lists the electrotonic coupling strengths for the two subnetwork system in Section 6. These values were chosen from a uniform distribution that spanned the range $[0.15, 0.2]$.

A.2. Parameters for the neuronal network of four subnetworks

For the four subnetwork system in Section 7, N=1000 neurons with 250 neurons in each subnetwork. The subnetworks are heterogeneous, with baseline stimuli $I_{b_i} \in [4.0, 4.8]$ μA/cm^2 for the first subnetwork, $I_{b_i} \in [4.8, 5.6]$ μA/cm^2 for the second subnetwork, $I_{b_i} \in [5.6, 6.4]$ μA/cm^2 for the third subnetwork, and $I_{b_i} \in [6.4, 7.2]$ μA/cm^2 for the fourth subnetwork, each drawn from a uniform distribution. Here, the noise intensity is taken to be $D = 0.0016$. The synaptic reversal potential of the synapse connecting presynaptic neuron j and postsynaptic neuron i depends on the subnetworks containing neurons i and j and can be found by referencing Table A.3. Note that neurons in the same subnetwork are not synaptically coupled.

The synaptic coupling strength between any two neurons i and j again depends on the subnetworks containing neurons i and j. Table A.4 lists the synaptic coupling strengths between neurons in the four subnetworks of Section 7. These values were chosen from a uniform distribution that spanned the range $[0.01, 0.08]$.

The electrotonic coupling strength between any two neurons i and j is the same for all neurons within that subnetwork. Table A.5 lists the electrotonic coupling strengths for the four subnetwork system in Section 7. These values were chosen from a uniform distribution that spanned the range $[0.15, 0.18]$.

Data availability

Data will be made available on request.

Table A.3
Table of synaptic reversal potentials (in mV) between the four 250 neuron subnetworks analyzed in Section 7. $E_{syn}(j,i) = 0$ mV yields an excitatory connection and $E_{syn}(j,i) = -100$ mV yields an inhibitory connection.

	$1 \le i \le 250$	$250 < i \le 500$	$500 < i \le 750$	$750 < i \le 1000$
$1 \le j \le 250$	–	−100	0	−100
$250 < j \le 500$	−100	–	0	0
$500 < j \le 750$	0	0	–	−100
$750 < j \le 1000$	−100	0	−100	–

Table A.4
Table of synaptic coupling strengths between the four 250 neuron subnetworks analyzed in Section 7.

	$1 \le i \le 250$	$250 < i \le 500$	$500 < i \le 750$	$750 < i \le 1000$
$1 \le j \le 250$	0	0.0101	0.0495	0.0235
$250 < j \le 500$	0.0101	0	0.0667	0.0509
$500 < j \le 750$	0.0495	0.0667	0	0.0436
$750 < j \le 1000$	0.0235	0.0509	0.0436	0

Table A.5
Table of electrotonic coupling strengths $K_{j\to i}$ between any two neurons i and j for the four 250 neuron subnetworks analyzed in Section 7.

	$1 \le i \le 250$	$250 < i \le 500$	$500 < i \le 750$	$750 < i \le 1000$
$1 \le j \le 250$	0.1500	0	0	0
$250 < j \le 500$	0	0.1669	0	0
$500 < j \le 750$	0	0	0.1558	0
$750 < j \le 1000$	0	0	0	0.1743

References

[1] Eric Brown, Jeff Moehlis, Philip Holmes, On the phase reduction and response dynamics of neural oscillator populations, Neural Comput. 16 (4) (2004) 673–715.
[2] John Guckenheimer, Isochrons and phaseless sets, J. Math. Biol. 1 (1975) 259–273.
[3] Eugene M. Izhikevich, Dynamical Systems in Neuroscience, MIT Press, 2007.
[4] Yoshiki Kuramoto, Chemical Oscillations, Waves, and Turbulence, Springer-Verlag, Berlin, 1984.
[5] Hiroya Nakao, Phase reduction approach to synchronisation of nonlinear oscillators, Contemp. Phys. 57 (2) (2016) 188–214.
[6] Arthur T. Winfree, Patterns of phase compromise in biological cycles, J. Math. Biol. 1 (1) (1974) 73–93.
[7] Bastian Pietras, Andreas Daffertshofer, Network dynamics of coupled oscillators and phase reduction techniques, Phys. Rep. 819 (2019) 1–105.
[8] Bharat Monga, Dan Wilson, Tim Matchen, Jeff Moehlis, Phase reduction and phase-based optimal control for biological systems: a tutorial, Biol. Cybernet. 113 (1) (2019) 11–46.
[9] Bard Ermentrout, David Hillel Terman, Mathematical Foundations of Neuroscience, vol. 35, Springer, 2010.
[10] Peter Ashwin, James W. Swift, The dynamics of n weakly coupled identical oscillators, J. Nonlinear Sci. 2 (1992) 69–108.
[11] Arthur T. Winfree, The geometry of biological time, in: Interdisciplinary Applied Mathematics, Springer New York, 2001.
[12] Dan Wilson, Jeff Moehlis, Isostable reduction of periodic orbits, Phys. Rev. E 94 (5) (2016) 052213.
[13] Dan Wilson, Phase-amplitude reduction far beyond the weakly perturbed paradigm, Phys. Rev. E 101 (2) (2020) 022220.
[14] Kaitlyn Toth, Dan Wilson, Control of coupled neural oscillations using near-periodic inputs, Chaos: An Interdiscip. J. Nonlinear Sci. 32 (3) (2022).
[15] Leon Glass, Michael C. Mackey, From Clocks to Chaos: The Rhythms of Life, Princeton University Press, 1988.
[16] Theoden Netoff, Michael A. Schwemmer, Timothy J. Lewis, Experimentally estimating phase response curves of neurons: theoretical and practical issues, Phase Response Curves Neurosci.: Theory Exp. Anal. (2012) 95–129.
[17] Peter J. Schmid, Dynamic mode decomposition of numerical and experimental data, J. Fluid Mech. 656 (2010) 5–28.
[18] J. Nathan Kutz, Steven L. Brunton, Bingni W. Brunton, Joshua L. Proctor, Dynamic Mode Decomposition: Data-Driven Modeling of Complex Systems, SIAM, 2016.
[19] Clarence W. Rowley, Igor Mezić, Shervin Bagheri, Philipp Schlatter, Dan S. Henningson, Spectral analysis of nonlinear flows, J. Fluid Mech. 641 (2009) 115–127.
[20] Joshua L. Proctor, Steven L. Brunton, J. Nathan Kutz, Dynamic mode decomposition with control, SIAM J. Appl. Dyn. Syst. 15 (1) (2016) 142–161.
[21] Maziar S. Hemati, Clarence W. Rowley, Eric A. Deem, Louis N. Cattafesta, De-biasing the dynamic mode decomposition for applied koopman spectral analysis of noisy datasets, Theor. Comput. Fluid Dyn. 31 (2017) 349–368.
[22] Steven L. Brunton, Joshua L. Proctor, J. Nathan Kutz, Discovering governing equations from data by sparse identification of nonlinear dynamical systems, Proc. Natl. Acad. Sci. 113 (15) (2016) 3932–3937.
[23] Niall M. Mangan, Travis Askham, Steven L. Brunton, J. Nathan Kutz, Joshua L. Proctor, Model selection for hybrid dynamical systems via sparse regression, Proc. R. Soc. A 475 (2223) (2019) 20180534.
[24] Jaideep Pathak, Brian Hunt, Michelle Girvan, Zhixin Lu, Edward Ott, Model-free prediction of large spatiotemporally chaotic systems from data: A reservoir computing approach, Phys. Rev. Lett. 120 (2) (2018) 024102.
[25] Zheng Wang, Dunhui Xiao, Fangxin Fang, Rajesh Govindan, Christopher C. Pain, Yike Guo, Model identification of reduced order fluid dynamics systems using deep learning, Internat. J. Numer. Methods Fluids 86 (4) (2018) 255–268.
[26] Alec J. Linot, Michael D. Graham, Deep learning to discover and predict dynamics on an inertial manifold, Phys. Rev. E 101 (6) (2020) 062209.
[27] Maziar Raissi, Deep hidden physics models: Deep learning of nonlinear partial differential equations, J. Mach. Learn. Res. 19 (25) (2018) 1–24.
[28] Dan Wilson, A data-driven phase and isostable reduced modeling framework for oscillatory dynamical systems, Chaos: An Interdiscip. J. Nonlinear Sci. 30 (1) (2020).
[29] Dan Wilson, A direct method approach for data-driven inference of high accuracy adaptive phase-isostable reduced order models, Phys. D: Nonlinear Phenom. 446 (2023) 133675.
[30] Talha Ahmed, Amir Sadovnik, Dan Wilson, Data-driven inference of low-order isostable-coordinate-based dynamical models using neural networks, Nonlinear Dynam. 111 (3) (2023) 2501–2519.
[31] Nancy J. Kopell, Howard J. Gritton, Miles A. Whittington, Mark A. Kramer, Beyond the connectome: the dynome, Neuron 83 (6) (2014) 1319–1328.
[32] Arosh S. Perera Molligoda Arachchige, The blue brain project: pioneering the frontier of brain simulation, AIMS Neurosci. 10 (4) (2023) 315.
[33] Mark W. Woolrich, Klaas E. Stephan, Biophysical network models and the human connectome, Neuroimage 80 (2013) 330–338.
[34] Julien Modolo, Alexandre Legros, Alex W. Thomas, Anne Beuter, Model-driven therapeutic treatment of neurological disorders: reshaping brain rhythms with neuromodulation, Interface Focus. 1 (1) (2011) 61–74.
[35] José M. Hurtado, Charles M. Gray, Laszlo B. Tamas, Karen A. Sigvardt, Dynamics of tremor-related oscillations in the human globus pallidus: a single case study, Proc. Natl. Acad. Sci. 96 (4) (1999) 1674–1679.
[36] Frederick A. Lenz, Hon C. Kwan, R.L. Martin, Ronald R. Tasker, Jonathan O. Dostrovsky, Y.E. Lenz, Single unit analysis of the human ventral thalamic nuclear group: tremor-related activity in functionally identified cells, Brain 117 (3) (1994) 531–543.

[37] Ron Levy, William D. Hutchison, Andres M. Lozano, Jonathan O. Dostrovsky, High-frequency synchronization of neuronal activity in the subthalamic nucleus of parkinsonian patients with limb tremor, J. Neurosci. 20 (20) (2000) 7766–7775.

[38] Lars Timmermann, Joachim Gross, Martin Dirks, Jens Volkmann, Hans-Joachim Freund, Alfons Schnitzler, The cerebral oscillatory network of parkinsonian resting tremor, Brain 126 (1) (2002) 199–212.

[39] Matthew D. Kvalheim, Shai Revzen, Existence and uniqueness of global koopman eigenfunctions for stable fixed points and periodic orbits, Phys. D: Nonlinear Phenom. 425 (2021) 132959.

[40] Alexandre Mauroy, Igor Mezić, Jeff Moehlis, Isostables, isochrons, and koopman spectrum for the action–angle representation of stable fixed point dynamics, Phys. D: Nonlinear Phenom. 261 (2013) 19–30.

[41] John Guckenheimer, Philip Holmes, Nonlinear Oscillations, Dynamical Systems, and Bifurcations of vector Fields, vol. 42, Springer Science & Business Media, 2013.

[42] Jan A. Sanders, Ferdinand Verhulst, James Murdock, Averaging Methods in Nonlinear Dynamical Systems, vol. 59, Springer, 2007.

[43] Herbert H. Jasper, Howard L. Andrews, Electro-encephalography: III. Normal differentiation of occipital and precentral regions in man, Arch. Neurol. Psychiatry 39 (1) (1938) 96–115.

[44] Miles A. Whittington, Roger D. Traub, Natalie E. Adams, A future for neuronal oscillation research, Brain Neurosci. Adv. 2 (2018) 2398212818794827.

[45] Edgar D. Adrian, Olfactory reactions in the brain of the hedgehog, J. Physiol. 100 (4) (1942) 459.

[46] John D. Green, Arnaldo A. Arduini, Hippocampal electrical activity in arousal, J. Neurophysiol. 17 (6) (1954) 533–557.

[47] John O'Keefe, Jonathan Dostrovsky, The hippocampus as a spatial map: preliminary evidence from unit activity in the freely-moving rat, Brain Res. (1971).

[48] Charles M. Gray, Wolf Singer, Stimulus-specific neuronal oscillations in orientation columns of cat visual cortex., Proc. Natl. Acad. Sci. 86 (5) (1989) 1698–1702.

[49] Miles A. Whittington, Roger D. Traub, John G.R. Jefferys, Synchronized oscillations in interneuron networks driven by metabotropic glutamate receptor activation, Nature 373 (6515) (1995) 612–615.

[50] Christian Bick, Marc Goodfellow, Carlo R. Laing, Erik A. Martens, Understanding the dynamics of biological and neural oscillator networks through exact mean-field reductions: a review, J. Math. Neurosci. 10 (1) (2020) 9.

[51] Jonathan E. Rubin, David Terman, High frequency stimulation of the subthalamic nucleus eliminates pathological thalamic rhythmicity in a computational model, J. Comput. Neurosci. 16 (2004) 211–235.